

Application of Electrochemical Impedance Spectroscopy to Degradation and Aging Research of Lithium-Ion Batteries

Published as part of *The Journal of Physical Chemistry* virtual special issue "Zhao-Wu Tian Festschrift".

Wenxuan Hu, Yufan Peng, Yimin Wei, and Yong Yang*



Cite This: *J. Phys. Chem. C* 2023, 127, 4465–4495



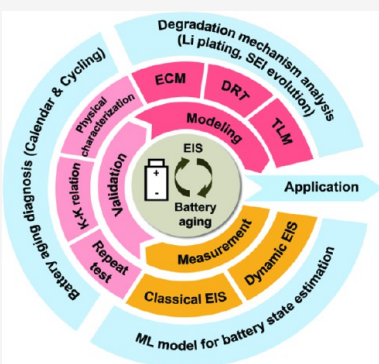
Read Online

ACCESS |

Metrics & More

Article Recommendations

ABSTRACT: An in-depth understanding of battery degradation and aging *in-Operando* not only plays a vital role in the design of battery managing systems but also helps to ensure safe use and manufacturing optimization of lithium-ion batteries (LIBs) in large-scale applications. Electrochemical impedance spectroscopy (EIS) is a nondestructive method which unravels electrode kinetic processes inside the batteries in different time domains, including charge-transfer reactions, interfacial evolutions, and mass diffusions. It has become a powerful diagnosis and pre/prognosis tool in battery aging research, as it provides important insight into the changes of internal electrochemical processes by correlating the impedance evolution to degradation mechanisms. This review gives a critical overview on rapidly developing impedance techniques for degradation and aging investigation of Li-ion batteries. The EIS variations of LIBs at different aging conditions of calendar aging and accelerated aging are systematically summarized. In addition, the working principles, data validation, and modeling methods, including equivalent circuit model (ECM), distribution of relaxation times (DRT), and transmission line model (TLM), of classical EIS and dynamic EIS are elaborately concluded. Finally, the challenges and perspectives of further application of EIS in the aging research of LIBs are presented.



1. INTRODUCTION

Nowadays, lithium-ion batteries (LIB) play a critical role in most aspects of human society due to their excellent energy storage performance. Since the LIB industry has flourished, the concerns of academia and industry have long been focused on how to develop and produce LIBs with better electrochemical performance on different scales. With the potential of electrode materials having been gradually exploited to the limit, an equally, if not more, important issue is brought to light, i.e., how to use these batteries efficiently and safely. To answer this question properly, an in-depth understanding of degradation mechanisms of LIBs in different operation conditions should be established.¹ Furthermore, monitoring the state of charge (SOC), state of health (SOH), and internal physicochemical parameters such as internal temperature/pressure plays a vital role in the diagnosis of the batteries. To achieve these targets, *in situ* or *operando* electrochemical and nonelectrochemical techniques are indispensable to detect the working state and degradation tendency of the battery accurately, which are still great challenges for battery researchers.

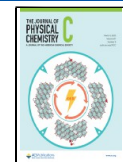
LIBs are a kind of complicated electrochemical system with several components, including cathode, anode, electrolyte, separator, and current collector. The complexity of the systems causes difficulties in decoupling and identifying the degradation mechanisms during battery aging. Recent rapid developments in large-scale applications of LIBs call for the systematic

understanding of the degradation mechanisms of LIBs, which highly depend on utilization and development of advanced characterization methods. X-ray-based techniques,² such as X-ray absorption spectroscopy (XAS), X-ray diffraction (XRD), and X-ray photoelectron spectroscopy (XPS), could determine the change of chemical composition and elements' valence and crystal structure. Electron and scanning probe microscopy techniques,³ such as scanning electron microscopy (SEM), transmission electron microscopy (TEM), and cryo-TEM, could observe the morphology change of the electrode and the thickness of solid electrolyte interface (SEI). Titration-based techniques, such as titration gas chromatography (TGC)⁴ and mass spectrometry titration (MST),^{5,6} could quantify the dead Li metal and SEI components. In addition, solid-state nuclear magnetic resonance (NMR)⁷ and electron paramagnetic resonance (EPR)⁸ are able to achieve a time-resolved and quantitative detection of Li plating. However, most of these methods are invasive technologies and need additional

Received: January 3, 2023

Revised: February 12, 2023

Published: March 1, 2023



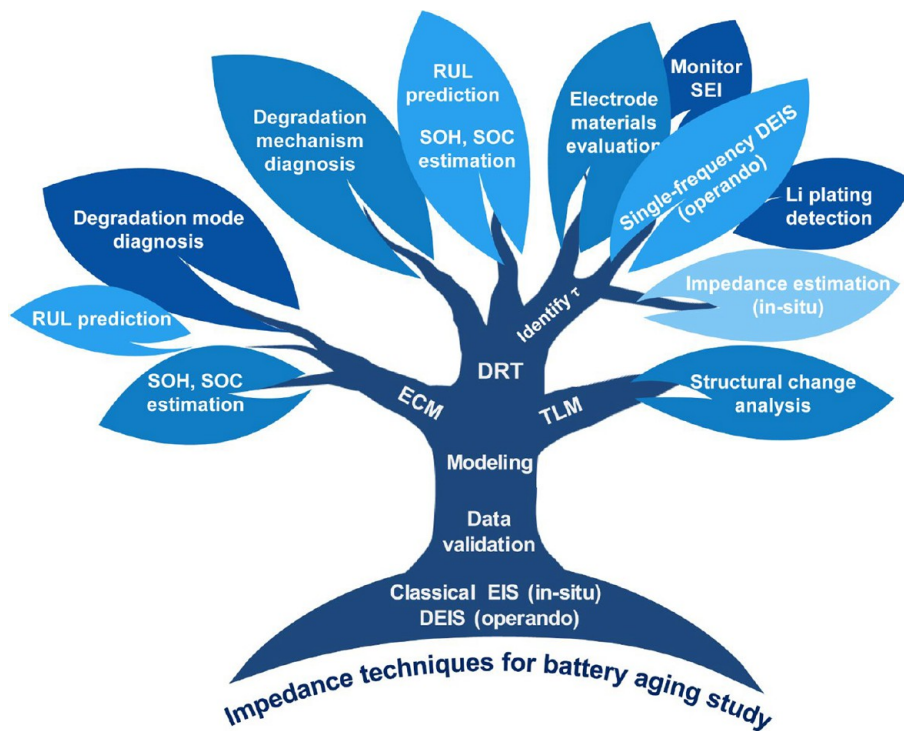


Figure 1. Schematic graph shows capability and custom procedures of electrochemical impedance techniques for the battery aging study.

expensive as well as precise instruments with special cell designs for tests, which are not feasible in practical application. Besides these physical characterizations, electrochemical methods, such as differential voltage analysis (DVA),^{9,10} differential charging voltage (DCV),¹¹ incremental capacity analysis (ICA),¹² and Coulombic efficiency (CE),^{13,14} also play instrumental roles in battery aging research. Nevertheless, they are quite complex determination methods that need a long monitoring time.

Electrochemical impedance spectroscopy (EIS) is a powerful tool in the analysis of electrochemical systems. By employing a sinusoidal current or voltage with a small amplitude as input signal, the electrochemical systems would generate an approximately linear response so that the impedance of cells over the time domain and frequency domain is obtained. Since the internal electrochemical processes in LIBs possess different relaxation times to respond to the perturbation, the impedance spectroscopy could detect convolutedly and be decoupled with different components by further modeling. Compared with physical characterization and other electrochemical characterization methods, EIS has several unique advantages. First, it relates voltage with current in the time domain and frequency domain so as to obtain the kinetic parameters of internal processes in LIBs. Second, it is a nondestructive technique, which is available in *in situ* and *operando* research. It can play an important role in monitoring the states of the battery during operation. Moreover, EIS could effectively deconvolute the complex electrochemical processes into a series of basic processes based on different relaxation times.¹⁵ The resolution of EIS is relatively high, especially with the assistance of new modeling methods, such as distribution of relaxation times (DRT),¹⁶ distribution function of differential capacity (DDC),¹⁷ and distribution of diffusion times (DDT).¹⁸ All of those characteristics make it possible to monitor the change in internal kinetic processes in LIBs by tracking the impedance

evolution and relating them to degradation mechanisms. Therefore, the EIS technique has been widely used in different applications for battery research, including internal temperature monitoring,¹⁹ degradation mechanism diagnosis,²⁰ battery states estimation,²¹ and remaining useful life (RUL) prediction.²²

There are several good reviews published which have concluded the principles, modeling, interpretation, and application of EIS in LIBs;^{23–31} e.g., Wang et al. provided a detailed method primer of EIS,²³ and Vivier et al. comprehensively elucidated the definition, graphical representation, error analysis, and application of electrochemical impedance.²⁴ When it comes to the interpretation of EIS data, there are mainly three types of methods, i.e., equivalent circuit model (ECM), DRT, and physics-based impedance model. Ciucci summarized different modeling approaches and their advantages and disadvantages.²⁵ Lu et al. introduced DRT methods in the views of the basic time scale property in batteries for battery diagnosis.²⁶ Gaddam et al. covered the physics-based modeling method and its application in different battery systems.²⁷ Other reviews in this area focused on the application of EIS to LIB research.^{28–31} McCarthy et al. provided a review on the use of impedance for assessing battery parameters of SOC, SOH, and internal temperature.²⁸ Wang et al. reviewed the onboard impedance acquisition, modeling, and applications under the premise of electric vehicle implementation.²⁹ While most of the present reviews focused on the EIS acquisition, modeling, and interpretation in different electrochemical systems, few of them have thoroughly summarized the application of EIS on degradation mechanism research of LIBs. Iurilli et al. concluded the EIS variations before and after cycling aging and calendar aging from the perspective of the battery chemistry based on ECM.²⁰ Though the review gives a critical assessment of EIS interpretation to model aging phenomena, the conclusion is mostly qualitative

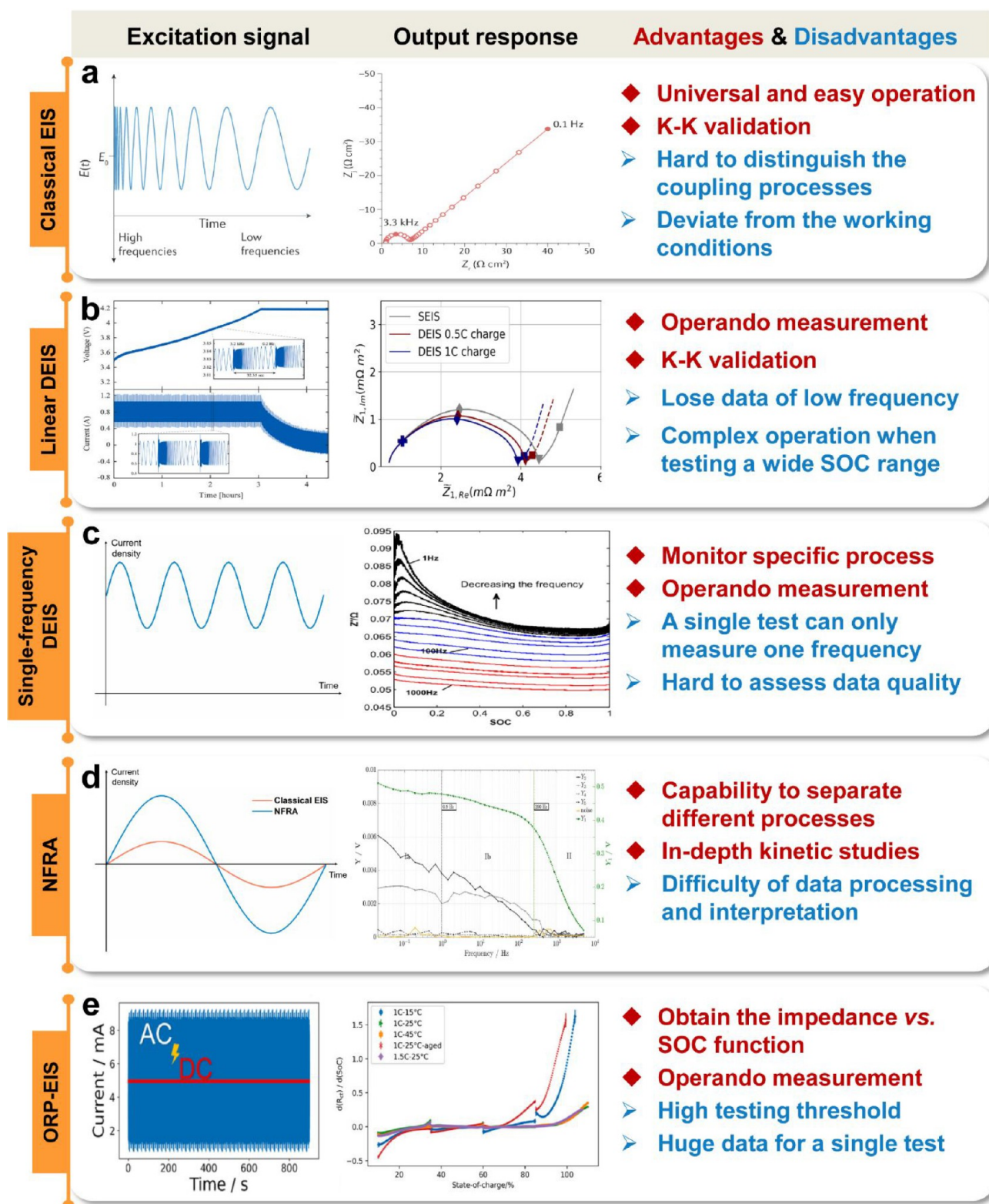


Figure 2. Excitation signals, output responses, advantages, and disadvantages of different impedance techniques: (a) classical EIS (reprinted with permission from ref 23. Copyright 2021 Springer Nature); (b) linear DEIS (reprinted with permission from ref 150. Copyright 2021 Elsevier. Reprinted with permission from ref 170. Copyright 2021 The Electrochemical Society); (c) single-frequency DEIS (reprinted with permission from ref 43. Copyright 2015 Elsevier); (d) nonlinear frequency response analysis (NFRA) (reprinted with permission from ref 50. Copyright 2017 Elsevier); (e) odd random-phase EIS (ORP-EIS) (reprinted with permission from ref 62. Copyright 2017 Elsevier).

due to the difficulty of deconvoluting EIS by ECM and the discrepancy in EIS results for the same battery chemistry between different references. To conclude, there is still a

vacancy for comprehensively summarizing the latest development of EIS applications for LIBs' degradation and aging research.

This review aims at providing a guideline for choosing and employing the appropriate impedance methods to achieve an in-depth study of the aging process of LIBs. In section 2, the working principles, measurements and data validation of classical EIS and dynamic EIS are elaborately overviewed. Section 3 focuses on the data modeling, interpretation, and general battery aging diagnosis procedure by ECM, DRT, and TLM. In section 4, the applications of EIS in the LIB aging study are comprehensively summarized in three aspects, including EIS variation at different battery aging conditions (calendar aging and accelerated aging), new impedance techniques for studying specific degradation mechanisms such as Li plating and SEI growth, and impedance-based machine learning model for battery states estimation. Section 5 gives a summary of this review and the perspectives of EIS application to battery degradation and aging research. The capabilities and custom procedures to employ different electrochemical impedance techniques for battery degradation and aging research are shown in Figure 1.

2. EIS MEASUREMENT

It is known that the classical EIS test is operated on the electrochemical system at a stable or quasi-potentiostatic state (e.g., open-circuit state), so as to obtain a time-invariant impedance spectrum. Moreover, a small perturbation amplitude should be applied to keep the formation of harmonics. Different from classical EIS, dynamic EIS (DEIS) that operates at nonstationary conditions is considered as a good alternative or auxiliary tool for unveiling the kinetics of complex electrochemical systems. In this section, the two major categories, classical EIS and DEIS, are presented in detail.

2.1. Classical EIS. 2.1.1. *Principle.* For the classical EIS, a sinusoidal potential or current signal with a small amplitude is used as the input signal as shown in Figure 2a. Based on the input signals, the classical EIS could be further divided into potentiostatic EIS (PEIS) and galvanostatic EIS (GEIS). While PEIS fulfills most of the requirements, GEIS is developed for the systems with low impedance, like commercial batteries, to avoid overflow. Although the input signals between GEIS and PEIS are different, the mechanism is the same, as shown in eqs 1 and 6. In a linear system, a sinusoidal potential signal at a specific frequency could lead to a sinusoidal current output at the same frequency with a phase angle (φ). Based on Ohm's law, the impedance of the electrochemical system at different frequencies could be obtained. By putting the result into a complex plane and employing Euler's formula, the impedance function could be transformed to the sum of real part (Z') and imaginary part (Z'').

Nyquist and Bode plots are now the most widely used methods to clearly display the features of impedance. By applying the real part of impedance to the x -axis and the negative imaginary part to the y -axis, a Nyquist plot, i.e., electrochemical impedance spectroscopy, is obtained to illustrate the variation of impedance over the frequency range. Although the Nyquist plot displays the features of real and imaginary parts of the impedance, it can not directly reflect the information on frequency unless marks are added in the figure. The Bode plot, as a supplementary Nyquist plot, takes the modulus ($|Z(\omega)|$, eq 5) and phase angle ($\varphi(\omega)$, eq 6) of the impedance as ordinate and logarithmic frequency as abscissa, which directly displays the information on frequency in graphs.

$$E(\omega) = |\Delta E| \sin(\omega t) \quad (1)$$

$$I(\omega) = |\Delta I| \sin(\omega t + \varphi) \quad (2)$$

$$Z(\omega) = \frac{E(\omega)}{I(\omega)} = \frac{|\Delta E| \sin(\omega t)}{|\Delta I| \sin(\omega t + \varphi)} = |Z(\omega)| e^{i\varphi} \quad (3)$$

$$Z(\omega) = |Z(\omega)| (\cos \varphi + i \sin \varphi) = Z'(\omega) + i Z''(\omega) \quad (4)$$

$$|Z(\omega)| = \sqrt{Z'(\omega)^2 + Z''(\omega)^2} \quad (5)$$

$$\varphi(\omega) = \tan^{-1} \frac{Z''(\omega)}{Z'(\omega)} \quad (6)$$

2.1.2. Data Validation. Since the quality of EIS data highly influences the modeling and interpretation process, data validation plays an important role in improving the credibility and reliability of EIS. To acquire reliable EIS data, three conditions should be sanctified, i.e., linearity, causality, and stability. Linearity means that the relation between the input signal and output response is linear. The impedance spectrum should be independent of the amplitude. However, the kinetic characteristic of the electrochemical process, described by the Butler–Volmer equation, is intrinsically nonlinear. Thus, a small amplitude of the perturbation signal should be employed to approach the linear situation. There are several experimental methods to conduct data validation, including varying the signal's amplitude to observe the consistency of impedance spectrum, comparing the value of total harmonic distortion (THD) with fundamental frequency, or recording the temporal response of the potential and current to make sure that the Lissajous curve is not distorted.³² Causality means the response of the system completely results from the inputs. Faraday cages can prevent the measured system from noises derived from an external electric field and electromagnetic waves. Stability means that the response is independent of time, which can be easily checked by repeated tests. Besides the above three measurement prerequisites, finiteness means the values of the imaginary and real parts of the impedance are finite over the frequency range. When the four conditions are met, the imaginary and real part of the complex functions satisfy the Kramers–Kronig (K–K) relations.³³ The expressions of the K–K relations are shown as follows:

$$Z'(\omega) = Z'(\infty) + \frac{2}{\pi} \int_0^\infty \frac{x Z''(x) - \omega Z''(\omega)}{x^2 - \omega^2} dx \quad (7)$$

$$Z''(\omega) = Z''(0) + \int_0^\infty \frac{\left(\frac{\omega}{x}\right) Z''(x) - Z''(\omega)}{x^2 - \omega^2} dx \quad (8)$$

$$Z''(\omega) = -\left(\frac{2\omega}{\pi}\right) \int_0^\infty \frac{Z'(x) - Z'(\omega)}{x^2 - \omega^2} dx \quad (9)$$

Considering the complexity of the calculation processes, several commercial and open-access software programs have been developed to help researchers achieve this work. Schönleber et al. developed the open-assess “Lin_KK” tool to conduct the K–K validity test.³⁴ By conducting the K–K transforms, the residuals between real and calculated values of every single point could be obtained based on eqs 10 and 11. Only if all of the residuals (residuals of the real part $\Delta_{Re}(\omega)$ and the imaginary part $\Delta_{Im}(\omega)$) are smaller than 1% can the EIS data be considered as credible.³⁵ Not until the raw data are

validated by K–K transforms can the researcher go through further data analysis and modeling.

$$\Delta_{\text{Re}}(\omega) = \frac{Z'(\omega) - \hat{Z}'(\omega)}{|Z(\omega)|} \quad (10)$$

$$\Delta_{\text{Im}}(\omega) = \frac{Z''(\omega) - \hat{Z}''(\omega)}{|Z(\omega)|} \quad (11)$$

2.2. Dynamic EIS. Since batteries are inherently nonlinear and unstable under operation, classical EIS measurement has been limited in LIBs' research. In practical tests, the cell would be charged or discharged to the specific SOC and then a classical EIS measurement would be conducted after relaxation, which is relatively time-consuming, inconvenient, and deflected from operation conditions. Therefore, a dynamic EIS (DEIS) technique has received more and more attention for its promising potential in *operando* techniques.

Based on the differences in the input signal, DEIS could be divided into two categories: linear time-varying (LTV) systems and nonlinear time-varying (NLTV) systems. In the LTV systems, the test conditions are often compromised so as to approximately fulfill the linearity of the EIS frequency response. The data analysis is still based on the linear framework of classical EIS, while in the NLTV systems the input signals are controlled to deliberately expose the nonlinear information on the processes in batteries. Since the linear framework of classical EIS is no longer suitable for these tests, different mathematical treatments, models, and frameworks are necessary to validate and interpret the results.

2.2.1. Linear Time-Varying Conditions. For the LTV conditions, the input current signal is usually the intermodulation of a direct current signal with an alternating current signal as shown in Figure 2b.^{36,150} In this way, the impedance under operation conditions rather than stationary conditions could be detected, which is helpful to unravel hidden kinetic mechanisms and parameters. It is worth noting that the frequency range used in linear DEIS usually discards the low frequency range to shorten the test time because the short test time could decrease the change of SOC during measurement to guarantee the data quality. The data of linear DEIS could also be validated by the K–K relations. Itagaki et al. first employed DEIS in LIBs to analyze the mechanism of Li⁺ intercalation into graphite and the formation of SEI.^{37,38} Huang et al. measured DEIS of a LiMn₂O₄/Li half-cell in the galvanostatic mode (0.1 mA alternating current) while the cell was charging or discharging at a series of direct currents (0.2–1.6 mA).³⁹ It is found that the charge-transfer resistance decreases with the rise of direct current, which can be explained by the Butler–Volmer equation. Moreover, the R_{ct} during the charge process is smaller than that during the discharge process at the same SOC. The underlying reason, proposed based on a single particle model, is attributed to a significant surface lithium-ion concentration variation caused by direct current. The phenomenon, called R_{ct} hysteresis, has also been reported in other works.^{40–42} In another work, the phenomenon is ascribed to the change in the Li⁺ concentration in the electrolyte, which increases during deintercalation and decreases during intercalation.⁴¹ In addition, Watanabe et al. also found that both the R_{ct} and the magnitude of the R_{ct} hysteresis increased with the particle size of cathode materials.⁴² They considered that the hysteresis of R_{ct} could

be an indicator of electrode materials with fast charge–discharge capability.

In addition to linear DEIS, single-frequency DEIS is another kind of technique for LTV conditions. As shown in Figure 2c, it uses an intermodulation signal with a single-sine current signal with a single frequency and a large direct current to observe the impedance variation of the specific frequency over a large SOC range during charging or discharging. Since SOC varies significantly during the measurement, the multi-frequency test is meaningless and inaccurate. Different from linear DEIS in which the SOC during measurement is nearly unchanged in a short test time, the single-frequency DEIS could be conducted over the whole SOC and closer to working conditions. Huang et al. first employed the single-frequency DEIS method to measure a continuous impedance change of LIBs with charge and discharge over a full SOC range.⁴³ A small ac current amplitude (0.01 A, 1% dc current) was used to meet the linear condition. However, the disadvantage of this method is that a single test could only obtain the impedance of a single frequency, which makes it inconvenient to get a full-frequency-range impedance spectrum. Therefore, its application scenarios should be delicately selected to maximize its advantages. Actually, the single-frequency DEIS has a unique advantage when investigating a specific process with a stable time constant, in which case the measured impedance variation could be ascribed to the process. Lyu et al. used single-frequency DEIS to find the indicator of predicting thermal runaway caused by overcharge.¹⁹ The impedance at 70 Hz is found to be correlated with overcharging as the slope of impedance evolution turns from negative to positive when the cell starts to overcharge. By online monitoring of the dynamic impedance at 70 Hz, the thermal runaway could be prevented by cutting off the charging once the slope turns positive. It provides a protocol for single-frequency DEIS application. It is better to use single-frequency DEIS with a selective frequency as an indication method for detecting specific degradation mechanisms.

2.2.2. Nonlinear Time-Varying Conditions. For the NLTV conditions, the output response deviates from the ideal linear framework owing to the nonlinear distortion. As a result, it is necessary to detect and quantify this deviation to evaluate the validity of impedance measurement and achieve data interpretation.⁴⁴ Nonlinear EIS can provide additional information to distinguish the physicochemical processes in certain cases where linear EIS is incapable, since the faradaic and nonfaradaic reactions show considerably different contributions to higher harmonics.⁴⁵ Nonlinear EIS has already been used in solid oxide fuel cells,⁴⁶ electrochemical reaction mechanisms,^{47,48} and electrocatalytic reactions.⁴⁹ However, only a few groups have been devoted to the research of employing the techniques for LIBs due to the complexity of battery chemistry and the difficulty of nonlinear EIS measurement and data analysis. At present, two kinds of methods have been proven to be feasible in LIBs, i.e., nonlinear frequency response analysis (NFRA) based on higher harmonic response and odd random phase electrochemical impedance spectroscopy (ORP-EIS) based on multisine excitations.

NFRA is an effective method to obtain dynamic information about nonlinear processes by investigating higher harmonic responses. It is known that a small sinusoidal perturbation could lead to a sinusoidal response of the same frequency (f) with a phase angle. But if a large amplitude perturbation is employed, the response would be the sum of sinusoids at f , $2f$,

Table 1. Symbols, Circuits, Figures in Complex Plane, and Physical Meanings or Applications of the Electrical Elements and Simple Equivalent Circuits

Element	Symbol	Figure	Application
Resistor			The element can represent ionic resistance of electrolyte, SEI resistance, and charge-transfer resistance between electrolyte and electrode.
Inductor			The element can represent impedance contributions related to wound wires/battery structure at high frequencies, and specific adsorption or degradation processes at low frequencies.
Capacitor			The charge accumulation/depletion occurring at the electric double layer between electrode and electrolyte could be considered as a capacitor.
Constant phase element			The CPE is used to match the deviation of the frequency response characteristics of an actual electrode from a pure capacitor due to the dispersion phenomenon.
Warburg element			Warburg impedance is caused by diffusion process, which is assumed to occur in the stagnant layer with infinite length.
RC-element			RC-element is used to simulate the ideal interfacial electrochemical process regardless of mass transfer.
ZARC element			ZARC element is used to simulate the realistic interfacial electrochemical process regardless of mass transfer.
RL-element			RL-element is used to simulate the inductance loop or semi-arc, which usually occur at mid and low frequency.
Randles circuit			Randles circuit is the typical model to simulate an interfacial electrochemical process.
Voigt circuit			Voigt circuit is used to simulate a series of interfacial electrochemical processes in series.

$3f$, etc., while the sinusoids of higher frequencies nf ($n \geq 2$) are called higher harmonics. For NFRA, a sinusoidal current with a large amplitude is used to excite the system, as shown in Figure 2d. Thus, the amplitude of individual higher harmonic Y_n and the sum of them $\sum_{i=2}^n Y_n$ can be obtained on the basis of the Fast Fourier Transform (FFT). The value of Y_n reflects the strength of the nonlinear responses of different processes. Generally, physical processes like ionic transport show a relatively weak nonlinear response, while the redox reactions, charge-transfer processes at heterogeneous interfaces, deliver strong nonlinear responses. Harting et al. investigated the amplitude and temperature dependency of higher harmonic responses as well as the impact of aging of LIBs with NFRA and EIS.⁵⁰ Although it is difficult for EIS to deconvolute the impedance of electrochemical reactions and the ionic transport process in the SEI, NFRA could separate them and distinguish their typical frequency range by a local minimum in Y_3 . Admittedly, NFRA is a powerful dynamic measurement method that allows in-depth kinetic studies and diagnosis in LIBs. Nevertheless, there are still some limitations of this method. First, it is more of a qualitative method than a quantitative method, as it usually gives a relatively broad frequency range convoluting a class of processes, such as diffusion or electrochemical reactions. In addition, the clear interpretation of spectra requires physical models of the electrochemical systems. A robust correlation between Y_n and certain physical meaning or physicochemical processes should be constructed if they are used as indicators for certain degradation mechanisms.^{52–57}

In addition to NFRA, ORP-EIS is another state-of-the-art *operando* impedance technique. It was developed by the research group from the Vrije Universiteit Brussel in 2004.⁵⁸ Not until recent years has it been successfully used for LIBs. The method is able to obtain the full-frequency impedance change of LIBs over a wide SOC range during normal operation. A specially designed broadband periodic odd random phase multisine excitation is imposed on a direct current to detect the impedance and the nonlinear distortions. The time series for odd random phase multisine currents are generated in MATLAB, then written to the text file, and finally applied through a potentiostat. Halleman et al. extended the theoretical framework of ORP-EIS to NLTV systems by developing a nonlinear distortion quantification method, which makes it possible for ORP-EIS to be applied in LIBs.^{59–61} Zhu et al. used ORP-EIS to study the continuous evolution of the charge-transfer resistance over SOC for a NMC/graphite coin cell during charging at different temperatures, C-rates, and SOH.⁶² Since the method delivers a continuous function of resistance and SOC, the differential function of $dR_{ct}/dSOC$ vs SOC is obtained in Figure 2e, where the aged cell showed a larger upward slope than the new cell at SOC range of 70–100%. Halleman et al. conducted ORP-EIS in a commercial potentiostat to monitor the impedance evolution of LIBs during charging and discharging.⁶³ It is found that the nonlinear contribution dominates at low SOC. The physical origins of the differences between classical EIS and *operando* EIS are also discussed. The *operando* ORP-EIS is a promising way to monitor the impedance in real-time during LIBs operation. Nevertheless, several challenges need to be overcome. First, both the testing hardware and data processing software of the system are specially designed and self-assembled. Second, the high threshold makes it hard to popularize at present, even in the lab. Last, the data obtained in

an *operando* ORP-EIS test is too massive to store in a commercial electrochemical station.

Apparently, varieties of DEIS techniques are very attractive, since they can disclose dynamic impedance variations and hidden kinetic mechanisms during operation. Nevertheless, researchers should be very careful when using these techniques, as the error derived from nonlinear and nonstationary states may lead to a misleading conclusion. The validity of the DEIS data needs to be assessed based on the basis of a robust theoretical framework.

3. EIS DATA ANALYSIS FOR GENERAL BATTERY AGING DIAGNOSIS

The interpretation of EIS data is the most important but also the hardest part of its application. When using a symmetric cell or three-electrode system to measure the EIS of a single electrode in LIB, the elementary processes that could be detected involve (1) transfer of electrons from current collector to active materials; (2) transfer of electrons across the composite electrode layer; (3) diffusion of ion through the electrolyte; (4) diffusion and migration of ions through the separator; (5) diffusion of ions in the porous electrode; (6) double-layer charging in the solid/electrolyte interface; (7) electrochemical insertion process; and (8) coupled diffusion of ion and electron inside the active material particles.^{15,64} Although EIS could distinguish these individual processes in a single spectrum in the ideal case, many of them would convolute and overlap with each other in the realistic measurement. Therefore, it is a critical issue to deconvolute the inside information and achieve an unambiguous interpretation of the EIS data by modeling. The battery aging could be diagnosed as different degradation modes or mechanisms by monitoring the impedance evolution during aging. Edge et al. identified five principal degradation mechanisms, i.e., SEI layer growth, lithium plating, structural decomposition of the positive electrode, and particle fracture at both electrodes.^{65,66} Furthermore, these degradation mechanisms couple with each other and lead to observable degradation modes at the cell level, including loss of lithium inventory (LLI), loss of active materials (LAM), conductivity loss (CL), and stoichiometric drift. In this section, the most commonly used modeling methods, ECM, DRT, and TLM, and their application for general battery aging diagnosis are introduced.

3.1. Equivalent Circuit Model. **3.1.1. Data Modeling.** ECM is the most widely used method to analyze the EIS data at present. It is an *a priori* method. The model should be constructed on the basis of the priori knowledge about the battery system and characteristics of the Nyquist plot. The electrical elements are supposed to relate to the individual physicochemical processes in the battery. By constructing ECM and using complex nonlinear least-squares (CNLS) to fit EIS data, the impedance of different electrical elements could be obtained. There are several fundamental electrical elements, including resistor (R), capacitor (C), inductor (L), constant phase element (CPE, Q) and Warburg (W). Table 1 shows the symbols, figures in complex plane, physical meanings of the electrical elements, and simple equivalent circuits.

Resistance, capacitance, and inductance are three types of fundamental electric behaviors that can be simulated by resistor, capacitor, and inductor. CPE is developed to rectify the deviation of realistic capacitance, which is also called capacitance dispersion. Its origin is still uncertain. Several

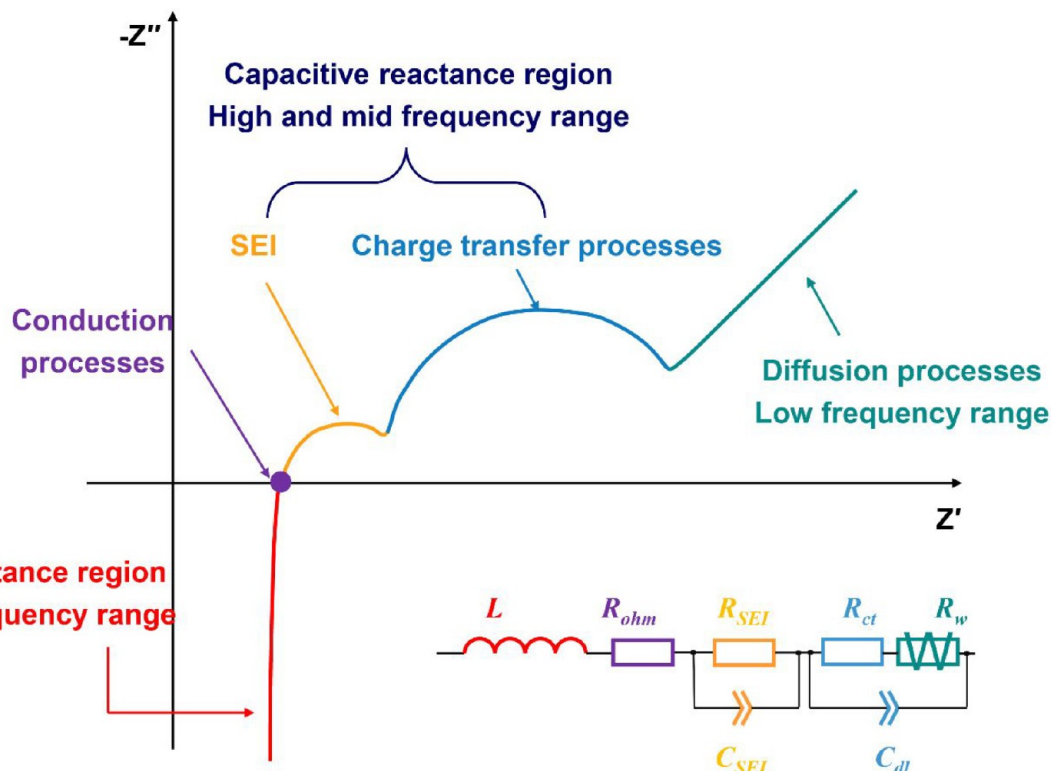


Figure 3. Typical Nyquist plot of LIBs and the dominant processes in different frequency ranges.

reasons have been discussed to cause the phenomenon, including nonuniform potential and current distribution, surface heterogeneity and roughness, and electrode porosity.⁶⁷ The figure of a capacitor in the Nyquist plot is a vertical ray with a 90° phase angle from the origin, while that of a CPE is a ray with a phase angle ranging from 0 to 90° from the origin. Warburg impedance is used to simulate the faradaic impedance resulting from the diffusion process. Due to the complexity of diffusion process, various types of Warburg impedance have been developed, such as semi-infinite diffusion, finite diffusion, spherical diffusion Warburg impedance, and so forth. Based on these electric elements, different ECMs could be constructed to fit practical electrochemical systems.

A typical Nyquist plot of commercial LIBs as shown in Figure 3 could be divided into three sections, the inductive reactance in the superhigh-frequency region, the capacitive reactance in the high- and midfrequency regions, and diffusion impedance in the low-frequency region. The second-order Randles circuit is usually used to fit this Nyquist plot. The corresponding electrochemical processes involved in each region are discussed in detail below.

At the superhigh-frequency region, the inductive signal appears at the fourth quadrant with a phase angle nearly -90° . It is commonly observed in those systems with small impedance, especially in commercial LIBs. The phenomenon derives from the porous structure of electrodes, an outer lead, and spirally wound electrodes. Simply deleting the data of the inductive section is not a good way, although this way is now widely used in EIS data processing. The presence of inductance could pull the first semicircle near the intercept of real axis down to the fourth quadrant. Therefore, deleting the range could lead to fitting error of the model parameter of the first semicircle. To maintain the accuracy of fitting results, a series inductor or an RL-element should be added in ECM to fit the inductance.

Despite high-frequency inductance, midfrequency and low-frequency inductance is relatively rare to see but also exists in LIBs.⁶⁸ Similarly, the low-frequency inductance arc could also be modeled by an RL-element coupled in a Randles circuit. At the border of superhigh- and high-frequency regions lies the intersection of the Nyquist plot and real axis, which represents the ohmic resistance of electrolyte and electrode. At high- and midfrequency regions, the capacitive reactance section is composed of several semicircles or semiarcs. Each semicircle represents a single electrochemical process, which can be described by an RC-element or a ZARC element. In general, the semicircles in the high- and midfrequency region are assigned to SEI and charge-transfer reactions of the cathode and anode, separately. At the low-frequency region, the diffusion impedance represents the diffusion process of ions in the solid phase, which is usually simulated by the Warburg element.

3.1.2. ECM for Degradation Mode Diagnosis. ECM exactly divides the Nyquist plot into several regions that are bound up with different degradation modes. By relating the impedance variations to the degradation modes, we can identify and quantify the batteries' internal evolution during aging can be identified and quantified. Specifically, the relationships in each region are shown as below:

In the high-frequency region, the increase of ohmic resistance (R_{ohm}) is generally ascribed to CL. To be specific, CL is mainly caused by electrolyte decomposition and consumption. Thus, the change of R_{ohm} is often used to reflect the degradation of the electrolyte. In addition, the corrosion of current collector and stripping of conductive carbon can also cause a loss of conductivity, though their proportions are small. At the midfrequency range, the first semicircle modeled by an RC element relates to SEI, with R_{SEI} representing Li⁺ diffusion ionic resistance and C_{SEI} representing the capacitance of the

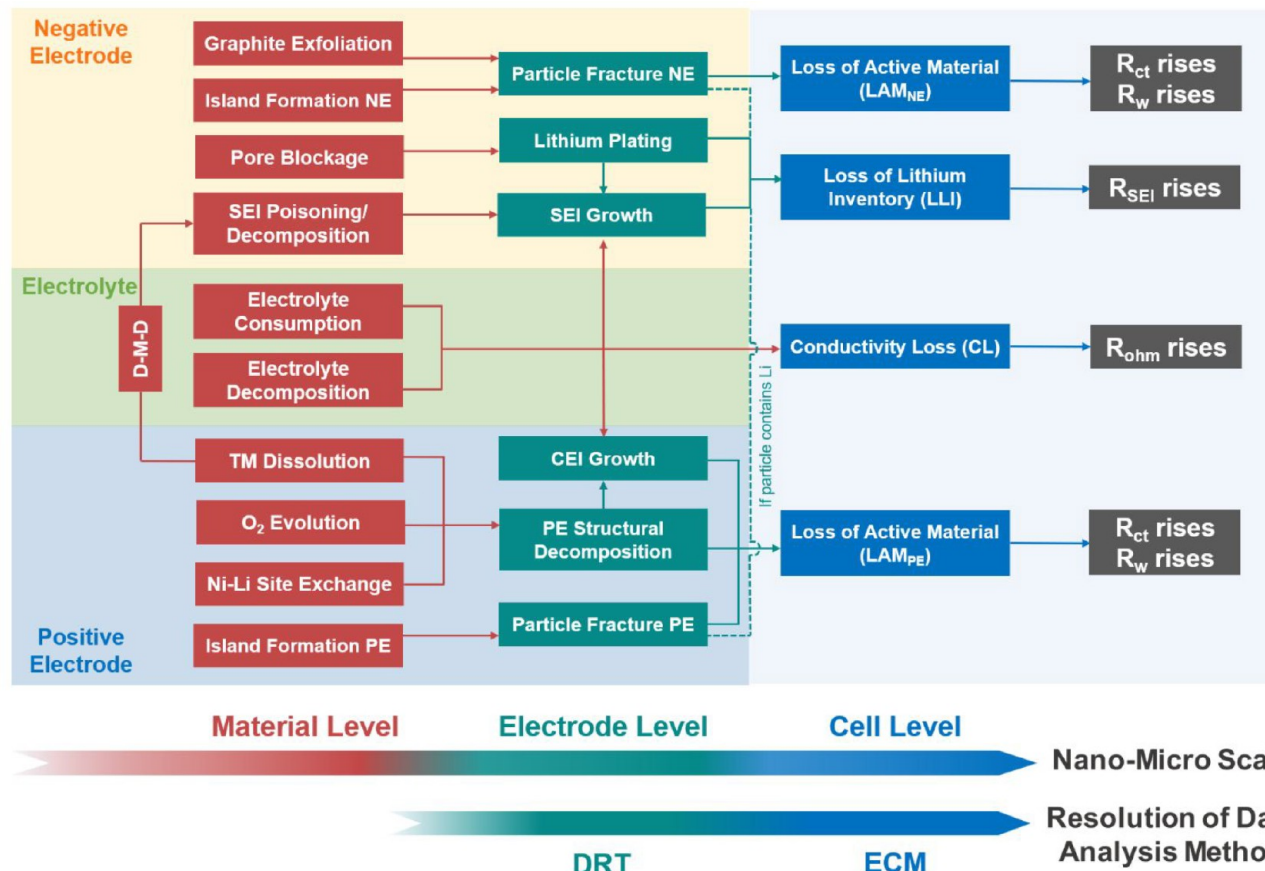


Figure 4. Coupling relationships between degradation mechanisms and modes and corresponding impedance evolution with the resolution capability of the data analysis methods (DRT and ECM). Reproduced with permission from ref 65. Copyright 2021 Royal Society of Chemistry.

SEI layer. The second semicircle modeled by an RC element relates to the charge-transfer reaction of the anode and cathode, with R_{ct} and C_{dl} denoting charge-transfer resistance and double-layer capacitance, respectively. However, the causes of the evolution of these elements are so complicated that they cannot be simply assigned to LLI and LAM. The coupling relationship between degradation mechanisms and degradation modes is shown in Figure 4. As the growth of SEI leads to LLI, the first semicircle is assigned to LLI. However, the second semicircle is influenced by several different degradation mechanisms, such as Li plating, structural decomposition of cathode, and particle cracking. It contains degradation mechanisms that lead to both LLI and LAM. In the low-frequency region, the increase of Warburg resistance (R_w) is caused by structural decomposition and particle fracture, which should be assigned to the LAM of both electrodes.

Based on the above analysis, it could be found that the point of controversy is the ascription of R_{ct} . In some studies, the sum of R_{SEI} and R_{ct} is assigned to LLI, while R_w is assigned to LAM.^{69,70} In the others, R_{SEI} is assigned to LLI, while the sum of R_{ct} and R_w is assigned to LAM.⁷¹ Recently, Iurilli et al. reviewed dozens of articles and concluded that R_{ct} was assigned to LAM in 61% of the cases.²⁰ The controversy is derived from the low resolution of ECM method since the second semicircle contains extensive information. The intrinsic limitation of the ECM makes this quantification method more of a rough evaluation than a precise calculation. In this review, the authors propound a proposal to assign the increase of R_{SEI} to LLI and

the increase of R_{ct} and R_w to LAM for two reasons. First, it has been reported that Li plating could lead to the decrease of R_{ct} of the anode.¹⁴⁵ Thus, assigning the increase in R_{ct} to LLI is not reasonable. Moreover, the plated Li would form SEI and dead Li, while Xu et al. employed DSC to quantify the two processes and found that the formation of SEI accounted for a larger proportion.⁷² Brown et al. also used the increased point of R_{SEI} as the onset of Li plating.⁷³ Therefore, the increase in R_{SEI} is able to reflect the degradation mechanisms of LLI, i.e., SEI growth and Li plating. Based on this proposal, the metric, G_{EIS} , is defined as the impedance growth in percentage to quantify the effects of degradation modes, as shown in eq 12.

$$G_{EIS} = \left\{ \begin{array}{l} CL (\%) = \frac{R_{ohm,n} - R_{ohm,0}}{R_{ohm,0}} \times 100 \\ LLI (\%) = \frac{R_{SEI,n} - R_{SEI,0}}{R_{SEI,0}} \times 100 \\ LAM (\%) = \left(\frac{R_{ct,n} - R_{ct,0}}{R_{ct,0}} + \frac{R_{w,n} - R_{w,0}}{R_{w,0}} \right) \times 100 \end{array} \right. \quad (12)$$

Despite being most commonly used in EIS data analysis and battery aging diagnosis, the ECM method has some inevitable limitations. First, there is no one-to-one correspondence between the ECM and kinetic behavior of the electrochemical system, which may lead to serious misinformation about

battery aging. Second, there is no one-to-one correspondence between ECM and EIS data as well. The ECM may vary with the state of battery aging (SOC, temperature, pressure, etc.), and a single EIS plot could be described by different ECMS. The option on different models is artificial to some extent. Furthermore, it is relatively hard for ECM to deconvolute the information between different kinetic processes with a similar time constant. The adjacent semiarch arcs usually overlap with each other in a practical test, preventing researchers from quantitative analysis and in-depth understanding about the battery systems. To overcome the difficulty and circumvent the shortcomings of ECM, several strategies are developed and proved to be effective,^{90–94} including the three-electrode system, symmetric cell, and distribution of relaxation times.

3.2. Distribution of Relaxation Times. DRT is a time-scale characterization that transforms the impedance of an electrochemical system from frequency domain to time domain. In the electrochemical system, the relaxation time of a single electrochemical process corresponds to its time constant. Time constant is an important concept in EIS, which represents the time that response signals attenuate to 1/e of its maximum. The physical meaning is the time that the system transits from the transient state to stationary state, reflecting the kinetic rate of the process. A larger time constant means a longer relaxation time. The relationship of the time constant, resistance, capacitance, and characteristic frequency (f_c , Hz) in a RC-element satisfies the following equation:

$$\tau = RC = \frac{1}{2\pi f_c} \quad (13)$$

For the same process in a certain electrochemical system, its time constant is determinate and nearly invariable, unless the component and structure of the interface have changed significantly. Each time constant corresponds to a single process in the system. Since different electrochemical processes have different time constants, DRT is able to separate, visualize, and quantify the various underlying electrochemical processes in the system. It could be considered as an upgraded successor to CNLS analysis.⁷⁴

3.2.1. Tikhonov Regularization. In principle, the DRT method is used to analyze the capacitance reactance part of EIS. Therefore, the pristine impedance spectrum should go through a data-preprocessing procedure to remove the inductive reactance and diffusion sections. One can use the inductor and Warburg element in ECM to fit the superhigh-frequency inductance and low-frequency diffusion process and then subtract the as-obtained value of the series inductance and Warburg element from the raw data to get the preprocessed data for further DRT analysis. In contrast to ECM, DRT is a model-free approach. It uses an infinite series of RC elements and ohmic resistance to fit the impedance spectra. Based on the assumption, the impedance could be expressed as eq 14, where R_p represents the total polarization resistance and $g(\tau)$ represents the distribution function of relaxation times. As the frequencies are often displayed logarithmically, a variable substitution shown in eq 16 is used to transform eq 14 to eq 17. Thus, the issue is to calculate the continuous function $G(\tau)$ on the basis of the finite impedance data. It is the so-called “ill-posed problem”, which means that $G(\tau)$ has more than one possible solution and is very sensitive to data noise.

$$Z(f) = R_0 + R_p \int_0^\infty \frac{g(\tau)}{1 + i2\pi f\tau} d\tau \quad (14)$$

$$\int_0^\infty g(\tau) d\tau = 1 \quad (15)$$

$$G(\tau) = \tau g(\tau) \quad (16)$$

$$Z(f) = R_0 + R_p \int_{-\infty}^\infty \frac{G(\tau)}{1 + i2\pi f\tau} d\ln \tau \quad (17)$$

To accomplish DRT calculations, several kinds of algorithms have been developed, including the Monte Carlo method,⁷⁵ Fourier transform,⁷⁶ genetic programming,^{77,78} and the most widely used Tikhonov regularization.^{79,80} Recently, new strategies such as deep neural network^{81,82} and the Gaussian process^{83,84} have also been developed and proved to be efficient and effective to realize DRT. Herein, the mechanism and effects of parameters in Tikhonov regularization are introduced.

There are two main processes in the Tikhonov regularization. First, the Gaussian function is used as the radial basic function to discretize $G(\tau)$. The reconstructed $G(\tau)$ could be written as eq 18, where x_m represents the weight coefficient and Φ_m represents the basic function in discretization. In other words, $G(\tau)$ is transformed to the weighted sum of numerous Gaussian functions centered on τ_m . x_m could be estimated by minimizing optimization function $S(\mathbf{x})$. As shown in eq 19,⁸⁵ the first term is the fitting residue term exhibiting the difference between experimental and modeled impedance, while the second term is the regularization term to obtain the optimal solution of \mathbf{x} , the vector of weight coefficient x_m ($\mathbf{x} = [x_1, x_2, x_3, \dots, x_m]$). A is a matrix consisting of $A_{n,m}$ as defined in eq 20.¹⁶ The product of $A_{n,m}$ and \mathbf{x} is the modeled impedance after discretization. In the regularization term, λ and $P(\mathbf{x})$ represent the regularization parameter and regularization function, respectively. The regularization parameter λ plays a vital role in the solution. A large regularization parameter leads to an oversmooth fitting result with peaks merged so that the independent processes cannot be separated properly. With λ decreasing, the smooth and wide peaks gradually become sharp and narrow. The overlapped characteristic peaks are also separate from each other. However, an excessively small λ can cause an overfitting problem. Recently, the L-curve method,⁸⁶ hyperparameter optimization,⁸⁷ particle swarm optimization algorithm,⁸⁸ and adaptive multiparameter regularization approach⁸⁹ have been developed to optimize the regularization parameter. Comparing the impedances reconstructed from the combination of inversion of DRT and ECM with the original data is also an important validation step.

$$G(\tau) = \sum_{m=1}^M x_m \phi_m(\ln \tau_m) \quad (18)$$

$$S(\mathbf{x}) = \|Z(f) - Ax\|^2 + \lambda P(\mathbf{x}) \quad (19)$$

$$A_{n,m} = \frac{1}{1 + j2\pi f_n \tau_m} \quad (20)$$

3.2.2. Peak Identification. Based on these algorithms, DRT profiles with several peaks distributed over the time domain could be acquired. Then the most important and difficult procedure is to assign DRT peaks to specific physicochemical

processes. When the battery chemistry is known and clear or the peak characteristics in DRT are simple, comparing the time constants of peaks with similar references could realize the peak identification. Since the time constant of a specific process is determined by the kinetic characteristic, it would vary within a relatively narrow range in the same battery chemistry. The variation may be attributed to the difference of the composition, purity, and structure of electrode materials or electrolyte. However, the method could not take effect when the battery chemistry is complicated and unclear or there are too many peaks. In that case, special strategies should be employed to separate the information on anode and cathode from the full cell's EIS.

Assembling anode and cathode half-cells to compare with full-cell is an available way to decouple their effects on a full cell's DRT profile. However, the lithium counter electrode would exert a negative influence on peak identification, as the peaks derived from SEI and the charge-transfer process of the lithium counter electrode may overlap other peaks. In contrast to the half-cell method, assembling the symmetric cells of cathode and anode is a feasible way to avoid the influence of lithium counter electrode.^{90–93} In addition, introducing a reference electrode to construct a three-electrode system is also a common strategy to directly obtain the impedance spectra of anode and cathode. In a recent review, Xiao et al. comprehensively summarized the design parameters and typical applications of reference electrodes in LIBs.⁹⁴ The materials, manufacturing, placement, and geometry of the reference electrode could influence the obtained results.⁹⁵ In order to minimize the artifacts, the settings of the reference electrode were carefully rationalized. Compared to a symmetric cell, the biggest advantage of three-electrode system is that EIS measurement could be operated at *in situ* conditions. However, there are still two limitations to the method. First, the stability of the reference electrode is not good enough to support long-term use. Thus, it is still a challenge to achieve *in situ* EIS measurement using the three-electrode system during battery aging. In addition, the configuration of the three electrode system for a large-capacity cell is still a difficulty, as the small reference electrode can cause a local current heterogeneity.

Besides the above strategies, controlling the measured conditions, such as temperatures or SOC, to distinguish peaks based on their different responsiveness is also a feasible method. Some of the processes in LIBs are temperature-dependent, while others are SOC-dependent. Some processes even occur only under specific testing conditions. Combining the physical meaning of processes with DRT peaks would help to realize accurate peak identification. For example, it is known that lithium–sulfur (Li–S) batteries have a complex cell chemistry due to the existence of polysulfides. Soni et al. combined a symmetric-cell strategy with a condition-controlled strategy to achieve an unambiguous identification of the eight peaks in the DRT plot.⁹⁶ Since polysulfides form gradually during the first discharge and appear at a specific voltage, the peaks from polysulfide can be determined by comparing cells in a fresh state or with different SOCs. Zhu et al. used DRT to analyze the EIS of commercial NMC-NCA/graphite batteries at different temperatures ranging from –5 to +25 °C. The resistance of the charge-transfer reaction hidden by SEI at room temperature is able to be distinguished at low temperature.⁹⁷ According to the different temperature dependency of time constants and resistances, the four peaks in DRT are assigned to particles/current collector contact resistance,

interfacial resistance of SEI, and charge-transfer resistance of anode and cathode. Moreover, the activation energy of different processes could be calculated based on the temperature-dependent EIS and eq 21, known as the Arrhenius law

$$\frac{1}{R_n} = Ae^{-E_a/rT} \quad (21)$$

where R_n , A , E_a , r , and T represent the resistance of a random process in batteries, pre-exponential factor, activation energy, gas constant, and temperature.

3.2.3. DRT for Degradation Mechanism Diagnosis. DRT is a better tool to do battery aging diagnosis than the ECM method. As it could deconvolute the impedance of the anode and cathode from total EIS spectra of the battery, a degradation mechanism level diagnosis could be achieved. After peak identification, the complicated EIS plot could be deconvoluted to several individual peaks belonging to a certain kinetic process. The integral areas of peaks represent the resistance of corresponding processes. By monitoring the variation of the peaks, the contribution of different degradation mechanisms on battery aging could be quantified. Iurilli et al. compared commercial NMC/graphite full cells and anode/cathode half-cells at the beginning and end of life to build a relationship between the impedance and different degradation mechanisms.⁹⁰ Except the peak with $\tau < 10^{-3}$ s assigned to electric and magnetic effects which shows no contribution to degradation, the changes of other five peaks in the full cell's DRT profiles are assigned to the different degradation mechanisms, including SEI growth/Li plating ($10^{-3} \text{ s} < \tau < 10^{-2} \text{ s}$), cathode particle cracking (two peaks, $10^{-2} \text{ s} < \tau < 10^{-1} \text{ s}$ and $10^{-2} \text{ s} < \tau < 10^{-1} \text{ s}$), graphite degradation ($1 \text{ s} < \tau < 10 \text{ s}$), and kinetic slow down ($\tau > 10 \text{ s}$). Zhou et al. combined DRT with a physical-based model to give a quantitative analysis of the contribution from different sources on power fade of LIBs aged under high-temperature cycling.⁹⁸ The evolution of the polarization resistance of different processes during battery aging is distinctly provided, which finds that the low-frequency diffusion polarization played a dominant role and accounted for 48% of the total growth in the polarization resistance. Moreover, the simulated voltage profile based on DRT results and eq 22 fits the experimental data well.

$$U_t = U_0 - IR_0 - I \int_0^\infty (1 - e^{-t/\tau}) \gamma(\tau) d\tau - \frac{It}{C_{in}} \quad (22)$$

where U_t and U_0 represent the terminal voltage and initial open-circuit voltage and I is the discharge current. The voltage loss of ohmic resistance, an individual polarization process and SOC change are calculated as IR_0 , $I \int_0^\infty (1 - e^{-t/\tau}) \gamma(\tau) d\tau$ and $\frac{It}{C_{in}}$, respectively.

Although DRT possesses great advantages in EIS data interpretation and battery-aging diagnosis, there are some issues that should be paid attention to when using DRT. Due to its high-resolution, a small noise or error in the primary EIS data could lead to a large deviation in DRT and misunderstanding about physicochemical processes in batteries. Thus, the quality of the primary data must be validated by K–K relations before further analysis. In addition, the pseudopeak formed during DRT calculation is another thorny problem that may lead to incorrect modeling results. Wang et al. discussed the types, origins, and factors of pseudopeaks in DRT.⁹⁹ The pseudopeaks could be sorted into three types: (1)

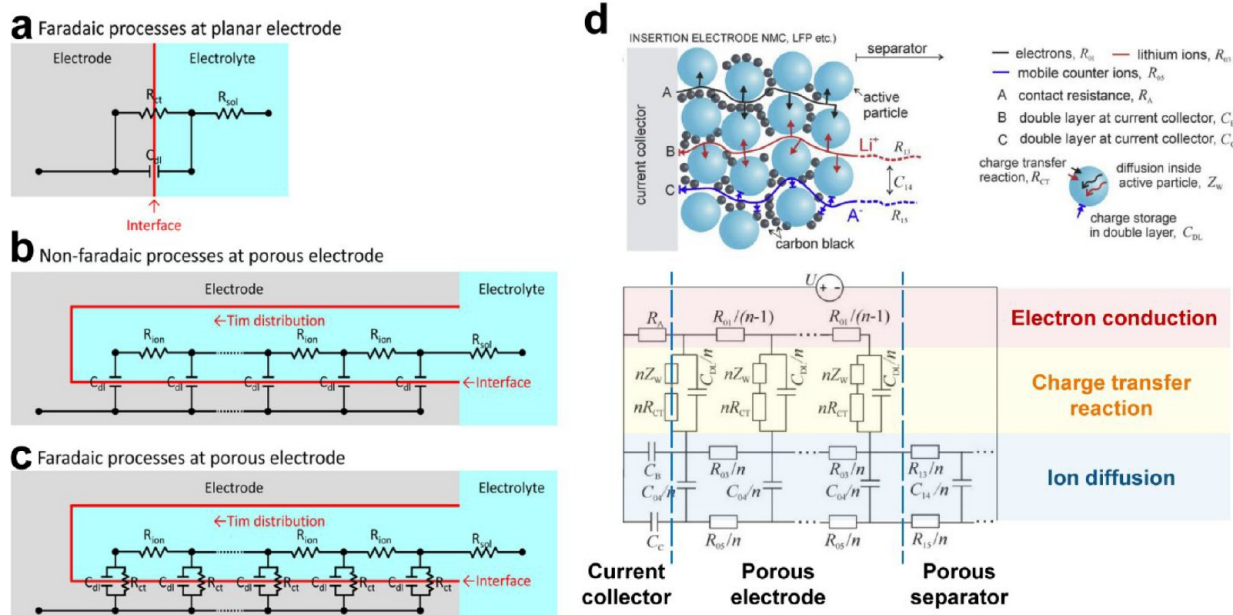


Figure 5. (a–c) Schematic diagram of the interfacial reactions in different electrodes and their electrochemical models. Reprinted from ref 107. Copyright 2015 American Chemical Society. (d) Typical physicochemical processes in a LIBs electrode and the physics-based transmission line model. Reprinted with permission from ref 101. Copyright 2021 Elsevier.

artificial peaks due to an overfitting problem; (2) missing peaks due to an underfitting problem, and (3) shifted peaks. The regularization parameter, uniformity of peak intensity, and impedance model are related to the generation of pseudopeaks. Simulating impedance spectra from integer to fractional-order models, which means splitting the whole spectrum, may be a good way to deal with the pseudopeak issue. However, there is still lack of a simple and effective method or standard to evaluate the degree of overfitting in DRT. To sum up, further development of new algorithms to improve the accuracy of DRT, decrease the artifacts caused by artificially choosing fitting parameters, and even achieve a one-click modeling procedure plays a crucial role in better application of DRT.

3.3. Transmission Line Model. TLM is a physical model used to treat the impedance issue of the porous electrode. For a simple electrode/electrolyte interface, the electrochemical behavior is described by a series-connected RC-element and resistance of solution (Figure 5a). However, there is an assumption of the circuit that the interface could be regarded as a uniform and continuous plane, which is not always the case for LIBs. TLM considers the entire interface of the porous electrode as the continuum of an infinite conjoint small interface. The small interface contains three physicochemical processes, including electron conduction in electrode, ion conduction in electrolyte, and interface reaction. Figures 5b,c shows the corresponding TLMs of different interface reactions (nonfaradaic processes or faradaic processes). Each RC element simulates the electrochemical reaction occurring on the nanometers of the total pore surface.¹⁰⁰ Moreover, the RC element has different time constants, suggesting the different time scale characteristics of the pore surface. Therefore, TLM can estimate the depth of electrochemical accessibility and the electrochemical accessible surface area of the porous electrode or thick electrode. Figure 5d exhibits the schematic of typical processes during Li⁺ intercalation and the TLM with the corresponding physical meaning. According to the interfaces in the electrode, the schematic could be divided into three

sections, the electron conduction and ion diffusion in the current collector/electrolyte interface, porous electrode/electrolyte interface, and the porous separator/electrolyte interface. In addition, the model could be simplified to the de Levie model by removing C_{04} and C_{14} when the diffusion of electrolyte in the pores and separator could be neglected. Moškon et al. discussed the calculative process of resistance in the TLM.¹⁰¹ Several commercial and open-access software programs have also been developed to help achieve the simulation based on TLM.^{102–104}

TLM possesses significant advantages in assessing the resistance of ionic diffusion (R_{ion}) in porous electrodes and extracting the parameters of ionic conductivity in the electrode. Therefore, it is a powerful tool to investigate the effects of structural decomposition during battery aging, such as changes of pore volume and tortuosity in the electrode. Nara et al. compared the fitting results of a conventional Randles circuit and TLM in LIBs, which found that TLM exhibited better fitting accuracy.¹⁰⁵ Moreover, R_{ion} could reflect the volume change of active materials during aging effectively. Bernard et al. used TLM to evaluate the influence of electrochemically blocking pores during cycling and calendar aging of LIBs. A noticeable polarization of anode at low frequency after aging indicates that the decreased porosity caused by SEI growth and gas bubble formation also plays a major role in battery aging.¹⁰⁶

4. APPLICATION OF EIS TO LIB'S AGING STUDY

4.1. EIS Variations at Different Aging Conditions. In this section, the effects of calendar aging conditions (SOC, temperature, battery chemistry) and accelerated stresses (temperature, charge/discharge rate, overcharging, etc.) on battery aging behaviors and the corresponding impedance evolution are systematically overviewed.

4.1.1. Calendar Aging. Calendar aging study is a critical but often overlooked issue in battery research. There are only about 500 reports in the latest 5 years when using the term

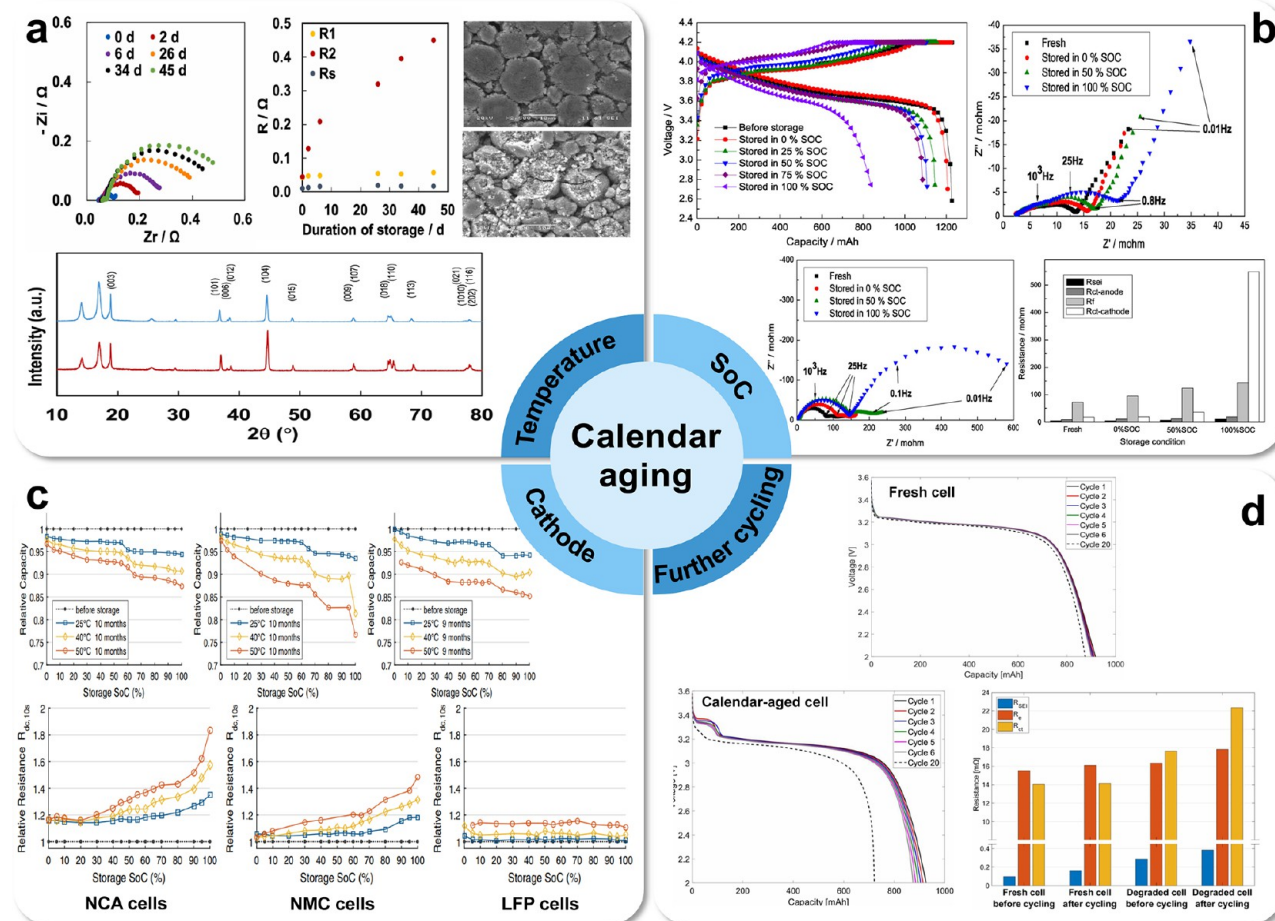


Figure 6. Calendar aging conditions: (a) Temperature: variation of EIS of calendar-aged cells over storage time. Changes in microstructures and XRD patterns of the cathode material. Reprinted with permission from ref 109. Copyright 2021 Elsevier. (b) SOC: charge and discharge profiles of the calendar-aged cells. Nyquist plots for disassembled anodes and cathodes and simulation results. Reprinted with permission from ref 112. Copyright 2010 Elsevier. (c) Cathode: variation of capacity and internal resistance of different batteries stored at various SOC and temperatures. Reprinted with permission from ref 114. Copyright 2016 The Electrochemical Society. (d) Further cycling: discharge curves and EIS fitting results of the fresh cells and calendar-aged cells before and after cycling. Reprinted with permission from ref 117. Copyright 2019 The Electrochemical Society.

“calendar” and “battery” to search on Web of Science. Calendar aging means storage of LIBs without working. Since there is no electrochemical reaction happening, the performance degradation is caused by side reactions in the battery chemistry. To be specific, the main degradation mechanisms include electrolyte consumption and decomposition, SEI and CEI growth, transition-metal dissolution, and gas generation. The storing temperature, initial SOC, and battery chemistry significantly influence the calendar aging.¹⁰⁸ Although calendar aging is different from cycling aging, the basic usage of EIS to make battery aging diagnoses is the same. Both ECM and DRT are able to interpret the EIS evolution to unravel the internal change and degradation mechanisms of LIBs.

From the perspective of an application scenario, investigating the calendar aging behavior of LIBs at high SOC and high temperature has more practical significances. Du et al. evaluated the calendar degradation behavior of LiNiO₂-based LIBs by storing them at 80 °C and 100% SOC for different durations.¹⁰⁹ As shown in Figure 6a, both R_{ohm} and R_{SEI} show little change after 45 days of storage, while R_{ct} increases up to 10 times more than the fresh cell. The post-mortem analyses by SEM and XRD exhibit a cracked microstructure and lithium

deficiency in the lattice of the calendar-aged cathode material, indicating that the degradation of the cathode is the main degradation mechanism. Schmitt et al. studied the effects of temperature on the calendar aging behavior of NMC batteries by storing them at different temperatures (0, 20, and 45 °C) for 470 days.¹¹¹ The R_{ohm} and R_p change little at 0 °C storage but are linearly enhanced at high temperature. Moreover, the slopes show a positive correlation with temperature. Sabet et al. harnessed DRT to track the impedance evolution of commercial NMC cells stored at high temperature (35 and 45 °C) and SOC (80% and 100%) for 700 days.¹¹⁰ It is found that R_{SEI} and R_{ct} increase by 5.14 and 3.18 times under the conditions of 80% SOC and 45 °C. The rise of R_{ct} derives from the CEI growth and transition-metal dissolution, which is proved by the change of time constant and post-mortem physical analysis. Li et al. explored the influence of SOC on calendar aging by storing LCO batteries at 55 °C and different SOC for 100 days.¹¹² As shown in Figure 6b, the capacity loss gradually increases with the rise of SOC from 0 to 75%, while a capacity plunge appears at 100% SOC. It is found that both R_{SEI} and R_{ohm} of the anode show an approximate linear increase from 0 to 100% SOC, corresponding to the growth of a new SEI layer. As a comparison, R_{ct} of the cathode shows a

slow rise at low SOC but dramatically increases at 100% SOC. The post-mortem analysis indicates that the high reactivity of LCO at high SOC causes TM dissolution, CEI formation, and pore clogging. The research indicates that SEI growth dominates the calendar aging at low SOC, while degradation of cathode dominates the high SOC condition.

In addition to the calendar aging conditions, cathode materials also play important roles in batteries' stability of batteries in calendar aging. Geisbauer et al. conducted a comparative study on the calendar aging behavior of five different cathode materials by relating the capacity decay to the resistance increase of full cells. It is found that NMC and NCA show a great resistance increase at high temperature and SOC, while LFP exhibits the best stability with little resistance increase at different conditions.¹¹³ Keil et al. also studied the impacts of SOC and temperature on the calendar aging of three kinds of commercial LIBs with NMC, NCA, and LFP cathodes.¹¹⁴ As shown in Figure 6c, the internal resistance of NMC and NCA increases slowly at low SOC (<60%) but rapidly enhances at high SOC, while the resistance of LFP shows little variation at different SOC. The structural decomposition of the cathode and side reactions between the cathode and electrolyte in NMC and NCA batteries is much more severe than in LFP batteries. Kassem et al. stored LFP batteries under different temperatures (35, 45, and 60 °C) and SOC (30%, 65%, 100%) for 8 months. It is found that elevated temperature exerts a more serious negative effect on capacity than high SOC.¹¹⁵ Moreover, the R_p and R_{ohm} significantly increase after storage, while R_W only slightly increases, indicating that LLI (SEI growth) instead of LAM_{PE} is the main source of capacity fade. Nevertheless, the contribution of R_{SEI} and R_{ct} on the increase of R_p is still ambiguous because the time constants of Li⁺ diffusion in SEI and the charge-transfer reaction of LFP are so close that they are hard to separate by ECM. To figure out the issue, Zheng et al. disassembled the calendar aged LFP cell (55 °C, 100% SOC, 10 months) and reassembled half cells to investigate the impedance change of the cathode and anode.¹¹⁶ The R_{ct} of the cathode changes little, while the R_{SEI} and R_{ct} of the anode significantly increase. The post-mortem analysis shows that Fe deposition and SEI growth at elevated temperature and high SOC causes the loss of cyclable or "active" lithium and capacity decay.

Assessment of the influence of calendar aging on the further use (cycling aging) of LIBs is an important issue in practical application. But few studies have paid attention to it due to the difficulty in setting a uniform test protocol. Mendoza et al. compared the cycling performance of the fresh and calendar-aged LFP cells at -5 °C.¹¹⁷ As shown in Figure 6d, the calendar-aged cell possesses a characteristic of Li stripping in the discharge curves, accompanied by a more significant impedance rise than the fresh cell. The results indicate that the calendar aging process aggravates the Li plating of LFP batteries in low-temperature operation. Zhang et al. combined calendar aging and cycling aging to investigate the degradation mechanisms and quantify the effects of the stored procedure on cycling life.¹¹⁸ The NMC batteries are first stored at different temperatures (25, 60, 70 °C) and 100% SOC for 15 days and then cycled under normal conditions. It is found that the temperature of calendar aging exerts a great influence on the further cycling performance. The batteries without storage and stored at 60 °C show close enhancements of R_{SEI} and R_{ct} after the cycling test, while the battery stored at 70 °C exhibits

a 1× higher R_{SEI} and a 6× higher R_{ct} than the battery stored at 60 °C. The XRD, SEM, and XPS results indicate that cation disorder and thickened SEI as well as CEI contribute to the impedance change of calendar aging. As the R_{ct} increase dominates the impedance increase of the full cell, the polarization caused by cathode kinetics slowing down is identified as the primary effect of calendar aging on the further cycling life of LIBs. In another work, the time span of calendar aging is also proven to significantly influence the batteries' cycling performance.¹¹⁹ The batteries stored at 80 °C for 7 days show little influence on the cycling performance. However, the cycling aging of a battery is accelerated when the storage time is prolonged to 15 days. Thus, the test protocol of the combination of calendar aging conditions and cycling aging conditions is necessary since it can lead to considerably different results. Moreover, the influence of calendar aging on battery cycling performance appears more in R_{ct} than R_{SEI} . The calendar aging could accelerate the degradation of active material, while the SEI grown during calendar aging would not accelerate the SEI growth during cycling aging.

In summary, calendar aging-induced degradation mechanisms mainly include SEI growth, electrolyte consumption, and structural decomposition of positive electrode. Enhancing the temperature and SOC could markedly accelerate calendar aging, as a high temperature speeds the rates of side reactions up, and a high SOC increases the activity of electrodes. The impedance variations under different calendar aging conditions are concluded in Table 2. The difficulties of calendar aging study are not the impedance data interpretation or degradation mechanism diagnosis but sufficient space and channel resources and the protocols for calendar tests and reference performance tests. In a recent commentary, Dufek et al. provided strategies to handle the issues and guidance for data collection and test protocols of calendar aging study.¹²⁰ Moreover, coupling EIS with machine learning may be a promising method for calendar aging prediction.

4.1.2. Normal Accelerated Aging Protocols. In general, LIBs possess years of lifespan under normal working conditions. To assess the quality of LIBs, accelerated aging is a critical issue to measure batteries' lifespan in a relatively short time span. By employing accelerated stresses, such as high temperatures, high charge/discharge rates, overcharging, over-discharging, the end of life could be arrived in advance. However, the battery aging characteristics can dramatically deviate from the case under normal working conditions, especially under harsh accelerated conditions. Based on the types of stresses, accelerated aging could be divided into normal and abnormal accelerated aging. The former should fulfill the prerequisite that the dominant degradation mechanisms or modes change little compared with normal working conditions, and the deviation part could be quantified and compensated in the lifespan calculation. Since EIS could make an *in situ* quantitative degradation mechanism diagnosis, it is a necessary technique to assess the accelerated aging conditions.

The high temperature accelerates the kinetic processes while also increasing the speed of the side reactions. Jalkanen et al. used EIS to explore the impedance evolution of commercial NMC pouch cells at different cycling temperatures (room temperature, 45 °C, and 45 °C charge/65 °C discharge).¹²³ As shown in Figure 7a, the capacity of different batteries drops to 80% of the nominal capacity after 2600, 2000, and 800 cycles

Table 2. Calendar Aging Tests and Corresponding Impedance Change and Degradation Mechanism Diagnosis of Different LIBs

Battery chemistry	Temp (°C)	SoC (%)	Storage time (days)	Impedance change	Degradation mechanism	ref
Li(Ni,Mn) _{1-x} Co _x O ₂	80	100	45	R_{ohm} , R_{SEI} hardly change, while R_{ct} increases 10 times	Particle crack, TM dissolution, CEI growth	109
LCO	55	0–100	100	R_{SEI} and R_{ct} of the anode linearly increase with SOC, while R_{ct} of the cathode suddenly increases at 100% SOC	SEI growth dominates the low SOC condition, while degradation of cathode dominates the high SOC case	112
NMC	0–45	50, 100	470	Both R_{SEI} and R_p show a similar linear upward tendency while the slope increases with temperature	Particle crack, SEI growth, electrolyte consumption	111
NMC	35, 45	80	700	R_{SEI} and R_{ct} increase by 5.14 and 3.18 times under 80% SOC and 45 °C	SEI growth, TM dissolution, cation-mixing, CEI growth	110
NMC	75	90	133	R_{ohm} hardly changes while R_{ct} of graphite and NMC increases significantly. Moreover, a new semicircle, derived from CEI, appears at the EIS of degraded cathode	TM dissolution, CEI growth, structural decomposition	121
LMO	25, 40, 60	50	392	R_{ct} and R_{SEI} significantly enhance, while the anode contribution is larger than that of the cathode	SEI growth is the dominant cause, while kinetic slowing down of the cathode and anode is the minor reason	122
LFP	0–60	0–100	870	R_p and R_{sh} increase faster at high temperature and SOC. SOC only shows a distinctive accelerated effect at high temperature	LJL induced by SEI growth is the main cause, while LAM of cathode is the minor reason	115
LFP	55	100	300	R_{SEI} significantly increases, while R_{ct} of the cathode hardly changes	SEI growth, electrolyte consumption, Fe dissolution, and deposition	116
NMC	25, 60, 70	100	15	Only R_{ct} shows a clear increase after storage. The aged cells at 70 °C show a significant impedance rise in further cycling tests compared to the aged cells at 60 °C	cation disorder at high temperature storage degrades the cycling performance of batteries	118

for the three cycling conditions, respectively. Both the R_{ohm} and R_{ct} of all batteries show continuous upward tendencies, corresponding to continuous electrolyte consumption and crack-induced cathode degradation. The R_{SEI} of cells at room temperature and 45 °C first increases and then changes little, while the R_{SEI} of cells at 45/65 °C surges at around 500 cycles and keeps growing. The drastic impedance rise at 45/65 °C is attributed to Li plating caused by excessive cycling, electrolyte drying, and the growth of a thick and resistive SEI layer. Strehle et al. studied the degradation of the NMC cathode under 45 °C cycling tests, which found that the increase of R_{ct} was double that of the ambient temperature conditions.¹²⁴ It results from the faster kinetics for transition-metal dissolution and rearrangement, oxygen removal, and reconstructed surface of the cathode at the higher temperature. Zhu et al. found that high temperature accelerated the local overcharge reaction and uneven degradation of NCA cathode, as R_{ct} of the aged cathode from different locations exhibited a 10-fold difference.¹²⁵ High temperature accelerates battery aging by increasing the speed of SEI growth at the anode side, as well as the particle crack and structural decomposition at the cathode side.

Enhancing the charge and discharge rates is also a common method to accelerate aging, although their accelerated effects and mechanisms are quite different. Raj et al. investigated how charge current (from 1C to 8C) and varying SOC ranges (from 10% to 100%) affected the cycling performance of NMC batteries.¹²⁶ As shown in Figure 7b, the high charge rate with wide SOC range (4C/60% and 8C/30%) leads to serious Li plating, rapid increase of impedance, and capacity decay, while most cases show quasi-linear capacity decay and impedance rise caused by SEI growth. Thus, the impedance vs cycle number baseline (red dashed line in Figure 7b) is constructed to assess the accelerated aging conditions of whether Li plating has happened or not. Similarly, Mussa et al. found Li plating, impedance rise, and capacity plunge at 3C charging.¹²⁷ But when charging at 4C, the impedance of the cathode and anode is smaller than the conditions with lower charge rates, while the direct-current resistance of the full cell is much larger than them. The phenomenon results from serious gas evolution due to SEI and electrolyte decomposition. It could be determined that the battery would quickly degrade to end-of-life with a totally different aging process and degradation mechanism if the charge rate is too high. Zheng et al. used varying discharge rates from 0.5 to 3C to accelerate the aging of the NMC batteries.¹²⁸ As shown in Figure 7c, the capacity loss accelerates when the discharge rate increases to 3C, although all of them show a linear degradation tendency without distinct capacity plunge. The Nyquist plots of the batteries show a gradual increase of different impedances at the low discharge rates, while R_{ct} dramatically increases at a 3C discharge rate. The results indicate that the main causes for capacity attenuation changes from SEI growth and electrolyte consumption to structural damage of active materials with discharge rate elevated. Zhu et al. also observed a faster increase in R_{ct} and a moderate change in R_{SEI} at high discharge rates.¹²⁹ Obviously, enhancing the discharge rates would not lead to such a dramatic change of degradation mechanism as enhancing the charge rate does.

Moreover, coupling high temperatures with high charge/discharge rates is a promising way to be applied in accelerated aging protocols for fast lifespan measurement. Since the high temperature could accelerate the kinetics of processes, it

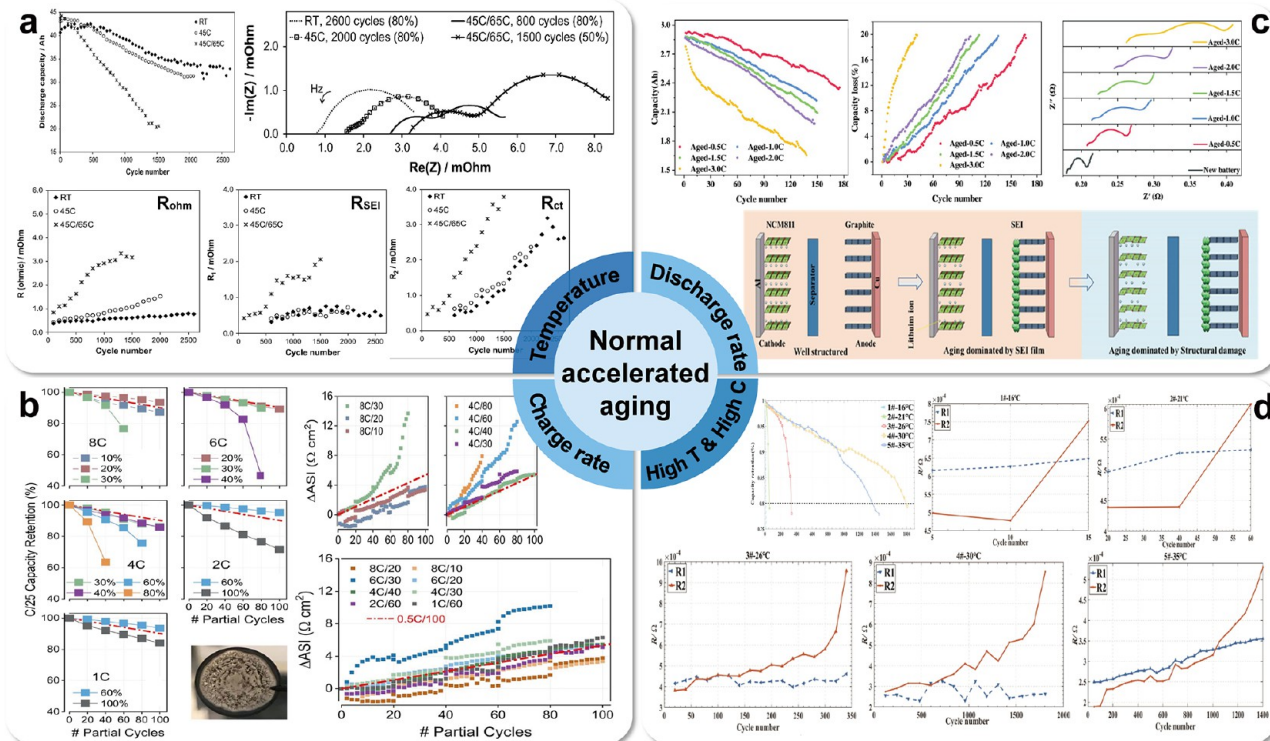


Figure 7. Normal accelerated aging stresses: (a) Temperature: variation of capacity, EIS, R_{ohm} , R_{SEI} and R_{ct} of batteries during cycling at different temperatures. Reprinted with permission from ref 123. Copyright 2015 Elsevier. (b) Charge rate: variation of capacity and impedance of batteries during cycling at different charge rates and SOC ranges. Reprinted with permission from ref 126. Copyright 2020 The Electrochemical Society. (c) Discharge rate: variation of capacity and EIS of batteries after cycling at different discharge rates; schematic diagram of the change of degradation mechanisms. Reprinted with permission from ref 128. Copyright 2022 John Wiley and Sons. (d) Coupling of high temperature and high charge rate: variation curve of capacity retention and impedance (R_1 and R_2 represent R_{ohm} and R_p , respectively) of batteries during cycling at different temperatures and charge rates. Reprinted with permission from ref 132. Copyright 2022 Elsevier.

expands the boundaries of available charge/discharge rates that fulfill the requirements for unchangeable degradation modes. Qu et al. evaluated the coupling effects of high charging rate (1, 3, 5C) to high temperature (25, 40 °C) on battery aging.¹³⁰ The capacity decay of batteries at high charge rate and 25 °C is quicker than that of batteries at high charge rate and 40 °C. The ICA and post-mortem analysis prove that Li plating occurs at 3C/25 °C, 5C/25 °C, and 5C/40 °C cycling conditions. The impedance evolutions of batteries aged at 5C/40 °C show that R_{SEI} and R_{ct} first change slightly and then increase significantly after 400 cycles, which corresponds to the Li plating-induced knee point. In addition, EIS could also be used to evaluate the accelerated effects of coupling high temperatures with frequency regulation protocols based on pulsed operations.¹³¹ Wu et al. used coupling accelerated conditions of different temperatures and 30 °C pulse charging to study the interplay of them.¹³² As shown in Figure 7d, the battery capacity plunges under low temperature due to Li plating. When the temperature is gradually increased, the evolutions of impedance show two stages, where R_p first slightly enhances and then drastically increases near the knee point. The two-stage aging behavior are attributed to SEI growth and Li plating, respectively.

4.1.3. Abnormal Accelerated Aging Protocols. At abnormal accelerated aging conditions, the aging processes are considerably deviated from normal cycling aging. Investigating these situations could help us understand the battery failure mechanisms and suppress the unexpected abnormal accelerated aging during battery working. It could

be found that enhancing the charge rate has a larger accelerated effect than enhancing the discharge rate, as a high charge rate could lead to Li plating. Actually, it is also an accelerated strategy to artificially let Li plating occurs. The available methods include high charge rate, overcharging, and temperature control. Rangarajan et al. operated cycling aging on commercial LCO batteries at different temperatures (-5, 22, and 40 °C), which found that the cells cycled at -5 °C lost 60% capacity in 15 cycles, and the cells cycled at 40 °C exhibited a hard knee point over 70 cycles, followed with swift capacity decay.¹³³ Both of the aging conditions lead to Li plating, and the mechanisms are different. In the low temperature condition, Li plating occurs at the initial cycle due to the slow intercalation kinetics. The anode impedance shows a continuous plating-induced rise resulting from the reaction between plated Li and the electrolyte, while at the high temperature, the anode impedance shows a slight increase during 30 to 70 cycles and surges after 70 cycles. The increased SEI resistance in the first stage causes a higher overpotential, resulting in Li plating that in turn accelerates porosity reduction and electrolyte consumption, further leading to a plating-induced rise of anode impedance. Carter et al. investigated the influence of the directionality of the interelectrode thermal gradient on the degradation mode by employing a ±2 °C temperature gap between the cathode and anode side.¹³⁴ As shown in Figure 8a, the batteries lose 77% capacity in 20 cycles when the anode is warmer than the cathode and 100% capacity when the cathode is warmer than the anode. The temperature gradient causes the imbalance of

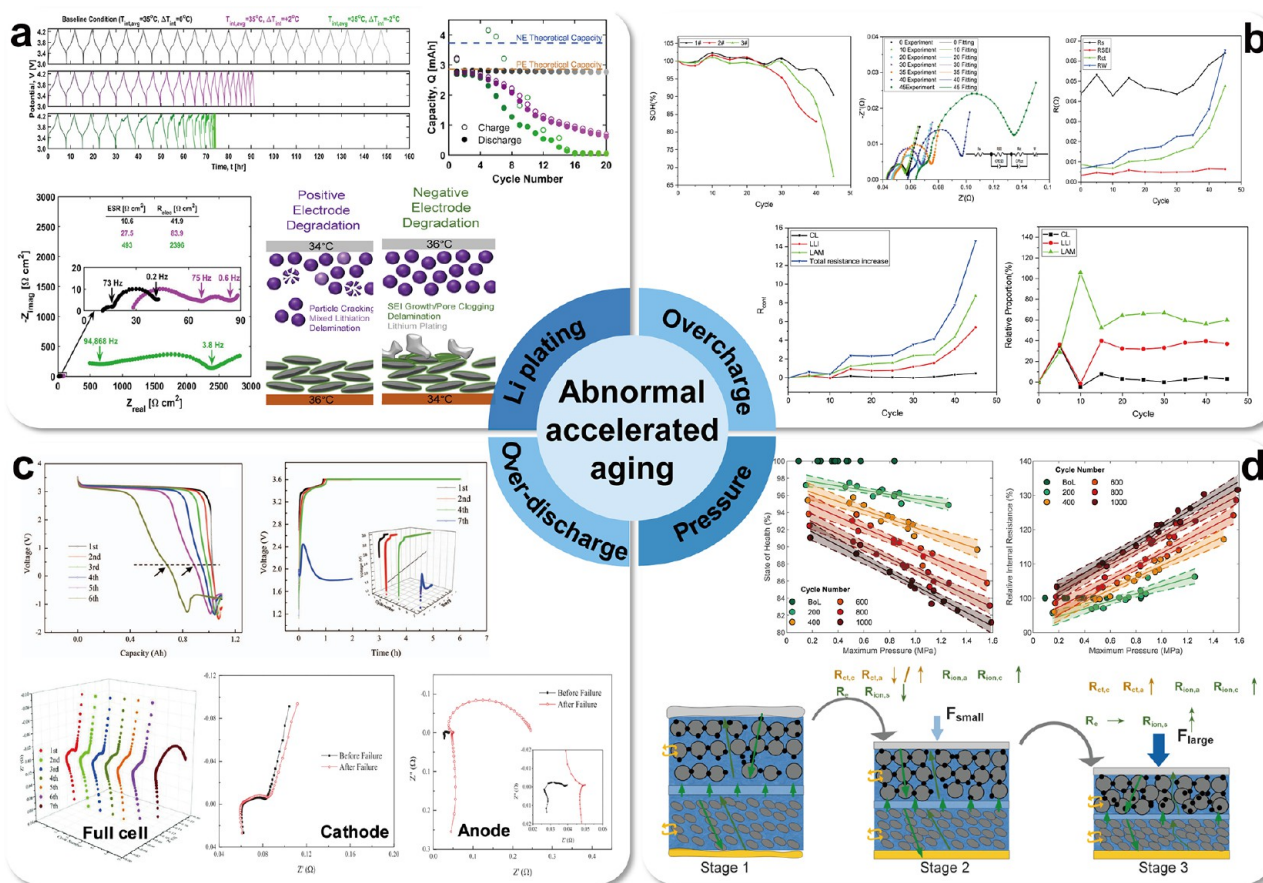


Figure 8. Abnormal accelerated aging stresses. (a) Li plating: cycling profiles and EIS of batteries after cycling. Schematic diagram of aging mechanisms for different thermal gradient conditions. Reprinted with permission from ref 134. Copyright 2021 Elsevier. (b) Overcharge: variation of capacity and EIS of batteries under overcharging cycling. Reprinted with permission from ref 135. Copyright 2020 Elsevier. (c) Overdischarge: variation of discharge and charge curves, EIS of full cell, anode, and cathode during 10% overdischarging cycles. Reprinted with permission from ref 138. Copyright 2014 The Electrochemical Society. (d) Pressure: correlation of SOH and internal resistance with pressure. Reprinted with permission from ref 139. Copyright 2021 Elsevier. Schematic illustration of the influence of pressure on impedance. Reprinted with permission from ref 140. Copyright 2022 Elsevier.

kinetics between cathode and anode. Based on the EIS degradation mode diagnoses, the higher temperature in the anode side exacerbates the normal degradation modes without changing their proportion severely, while the higher temperature in the cathode side accelerates Li plating, leading to a capacity plunge. Though Li plating could significantly accelerate battery aging, the degradation modes seriously deviate from the normal conditions. It is still hard to control Li plating in full cells by controlling the aging conditions.

Overcharging is supposed to cause Li plating, as well. But the capacity of an anode is always higher than the cathode in commercial batteries. The N/P ratio makes Li plating not so easy to occur at a normal charge rate. Liu et al. applied slight overcharge stress ($SOC \approx 118\%$) to commercial NCA batteries, which led to 70% capacity decay in 50 cycles.¹³⁵ As shown in Figure 8b, the aging process could be divided into three stages by tracking the impedance evolution and quantifying the proportion of different degradation modes based on the basis of eq 12. In the first stage, the degradation mode has no change to the normal conditions with a slow increase of all the resistance. In the latter two stages, the tolerance of cathode to high voltage gradually becomes weaker, and finally structure damage occurs. Thus, the proportion of LAM exhibits an accelerated rising tendency, which is the main

aging mechanism at overcharge conditions. Similarly, Togasaki et al. also found a two-stage aging process of NCA batteries at overcharge conditions ($SOC \approx 107\%$).¹³⁶ In addition, they used temperature-dependent EIS to separate the charge transfer resistance of the anode and cathode, which found that the metal deposition on the anode could cause significant change of resistance and capacitance of the anode. Liu et al. used a 10% overcharge condition to accelerate the aging of commercial LFP batteries, which also found the LAM of cathode dominated the aging mechanisms.¹³⁷

Overdischarging is another strategy to accelerate cycling aging. It can cause irreversible decomposition of the SEI and generation of gases, followed with the formation of a new SEI at the exposed fresh graphite surface. Liu et al. used EIS to investigate the failure of commercial LFP cells under overdischarging conditions.¹³⁸ As shown in Figure 8c, the batteries possessing 80% capacity retention after 1600 cycles rapidly failed after 49, 7, 3, and 1 cycles under 5%, 10%, 15%, and 20% overdischarge/normal charge cycling, respectively. It is found that R_{ohm} shows an upward tendency during aging, while R_{SEI} remained unchanged or fluctuated in the initial several cycles and suddenly increased before failed. The rise of R_{ohm} results from the corrosion of the current collector and continuous electrolyte consumption. The evolution of R_{SEI}

Table 3. Accelerated Aging Tests and Corresponding Impedance Change and Degradation Mechanism Diagnosis of Different LIBs

Accelerated Stress	Battery chemistry	Experimental conditions	Acceleration effects	Impedance change	Degradation mechanism	ref
Temperature	NMC/Gr	RT, 45, 45C/65D °C, 1C charge/discharge	The EOL decreases from 260 to 800 cycles	$R_{\text{sh}}^{\text{in}}$ and R_{et} keep a linear rise tendency, while R_{SEI} surges after 500 cycles	SEI growth, electrolyte drying, Li plating	123
	NMC/Gr	RT, 45 °C, 0.5C charge/discharge	The EOL decreases from 1000 (79% retention) to 700 cycles (67%)	The increase of R_{et} is double that of RT conditions and also much quicker than R_{ohm} and R_{SEI} .	TM dissolution, oxygen removal, reconstructed surface	124
Charge rate	NMC/Gr	30 °C, 1–8C charge, 0.2C discharge	The cells exhibited a quasi-linear decay, but the extreme high rate causes the capacity plunge	R_p first increases linearly and surges near the knee point	SEI growth (linear degradation region), Li plating (knee point)	126
	NMC/Gr	34 °C, 1–4C charge, 0.25C discharge	The 3C charge rate causes a capacity plunge, while 4C causes a quick failure	The R_p of the cathode and anode at 3C is the largest, while the direct current resistance of full cells at 4C is the largest	Li plating (3C), gas evolution (4C)	127
Discharge rate	NMC/Gr	25 °C, 0.5C charge, 0.5–3C discharge	The batteries show a linear capacity decay with slopes increasing with discharge rates	All impedance increases gradually at low C, while R_{et} dramatically enhance at 3C	SEI growth (0.5–2C), structural decomposition of cathode (3C)	128
Coupling condition (high T, high C)	NMC/Gr	25, 40 °C, 1–5C charge, 1C discharge	High temperature expands the available rates without Li plating (20 °C 3C and 45 °C 5C).	R_{SEI} and R_{et} show an accelerated increase tendency at high T and high C	SEI growth, Li plating	130
Overdischarge	LiFePO ₄ /Gr	105–120% DOD	The batteries rapidly fail in 7 cycles under 10% overdischarge	R_{SEI} fluctuated in the initial cycles and suddenly increased before failing, while R_{et} of cathode hardly changes	Electrolyte consumption, SEI decomposition/reformation	138
Li plating	NMC/Gr	temperature gradients (± 2 °C) between cathode and anode	The batteries quickly fail in 20 cycles	When anode is warmer, R_{ohm} and R_p increase by more than 2 times	Exacerbate normal degradation modes	134
	LCO/Gr	-5, 40 °C, 1C charge/discharge	Low T causes quick failure in 15 cycles, while high T leads to capacity plunge at 70 cycles	When cathode is warmer, R_{ohm} and R_p increase more than 50 times	Li plating, SEI growth	132
Overcharge	NMC/Gr	118% SOC	The batteries show a hard knee point at 30 cycles and then rapidly failure	R_p of anode shows a quasilinear increase at low T, while that shows a drastic rise near the knee point at high T	Li plating, SEI growth	132
	NCA/Gr	107% SOC	The batteries show a hard knee point at 100 cycles and then rapidly failure	$R_{\text{sh}}^{\text{in}}$ and R_{et} show a sudden rise at knee point, while RSEI hardly changes	Particle crack and structural decomposition of cathode	135
Pressure	NMC/Gr	0.66–1.98 MPa	The pressure at 1.32 MPa extends battery life, while too high or low pressure accelerates battery aging	$R_{\text{sh}}^{\text{in}}$ and R_p of cathode and anode increase with pressure changed, while the increase of R_w of the full cell is ascribed to graphite surface side-reactions	TM dissolution, particle crack and structural decomposition of cathode SEI growth, kinetic retardation, surface side-reactions	141

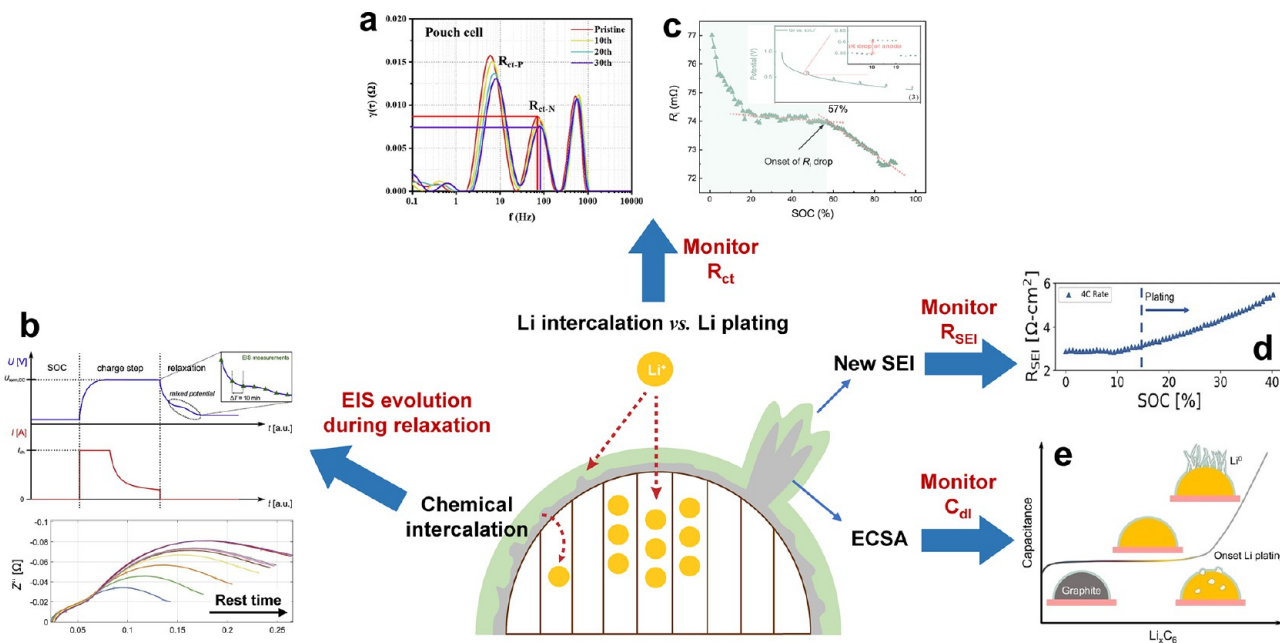


Figure 9. Schematic graph of impedance techniques for Li plating detection. (a) DRT results of batteries after the different number of cycles at 0 °C. Reprinted with permission from ref 145. Copyright 2021 Elsevier. (b) Schematic current and voltage profiles and the evolution of EIS during the voltage relaxation process. Reprinted with permission from ref 147. Copyright 2016 Elsevier. (c) variation of R_i over SOC, while the inflection point in the profile indicates the onset of Li plating. Reprinted with permission from ref 148. Copyright 2022 Elsevier. (d) Schematic illustration of R_{SEI} evolution during fast charging for the *operando* determination of onset Li plating. Reprinted with permission from ref 73. Copyright 2021 Elsevier. (e) Schematic illustration of dynamic capacitance measurement method for the *operando* determination of onset Li plating. Reprinted with permission from ref 151. Copyright 2022 Elsevier.

implies the decomposition and reformation processes of SEI, while the sudden increase is attributed to the largely forming nonconductive components. Moreover, with the impedance of the anode and cathode separated by a three-electrode system, it is found that the impedance increase of the anode dominates the impedance increase of the full cell, indicating that the change of SEI is the main degradation mechanism under overdischarging condition.

Besides the electrochemically accelerated stress, external pressure could also influence the lifespan of LIBs. Deich et al. exerted different external pressures on LIBs under cycling aging.¹³⁹ As shown in Figure 8d, the external pressure is positively and linearly correlated to the capacity fading rate and the impedance rising rate. However, Mussa et al. reported a "V" type relationship between battery lifespan and external pressure. The batteries show the longest cycling lifespan and smallest change of R_{ohm} and R_p after cycling at 1.32 MPa while further increasing the pressure results in a faster rate of impedance rise and capacity decay. Li et al. systematically concluded the influence of the pressure on battery impedance.¹⁴⁰ The appropriate pressure could help achieve the optimal porosity and good contact between the electrode and electrolyte with decreases in R_{ion} , R_{ohm} , and R_{ct} , while an excessively high pressure would reduce the contact area, leading to an accelerated increase of R_{ion} and R_{ct} .

The accelerated stresses could exert different effects on the battery aging process, leading to different degradation modes and impedance evolutions, which are summarized in Table 3. The normal accelerated aging conditions, such as coupled high charge/discharge rate and temperature, could linearly accelerate the capacity fade with little degradation mechanism change, so as to estimate the batteries' normal lifespan in a short time. The abnormally accelerated aging conditions

typically lead to rapid battery failures with different dominant degradation mechanisms. EIS could not only assess the boundary conditions of the normal accelerated aging protocols but also unravel the main cause and contributions of different degradation mechanisms on battery failure.

4.2. Degradation Mechanism Analysis. This section focuses on the impedance methods for investigating two main degradation mechanisms, Li platin, and SEI growth. The newly developed impedance techniques for detecting the onset boundaries of Li plating are summarized. The SEI growth monitoring based on the impedance evolutions during battery aging are also introduced as well as the physics-based SEI impedance model.

4.2.1. Li Plating. Li plating usually occurs when LIBs are charging at harsh operation conditions (such as fast charging, charging at low temperature, or overcharging) or undergo long-term cycles. When Li plating seriously occurs, the plated Li metal could puncture the SEI layer and react with the electrolyte to form a new SEI layer, leading to LLI and irreversible capacity loss. Moreover, since Li stripping during the discharge process generally happens near the surface of the anode, the tip of the Li dendrite would split away and form electrical isolated "dead Li". The detrimental Li plating can not only result in capacity fade but may also cause serious safety hazards. Therefore, developing a nondestructive, real-time way to monitor and quantify Li plating is of vital importance to develop methods to prevent it, improve LIBs' safety in use, and predict the RUL of LIBs. There have been many physical characterizations and electrochemical methods used to observe and quantify Li plating. Tian et al. compared the advantages and disadvantages of different detection methods for Li plating, which showed that EIS has no advantage over quantitative ness.¹⁴² Although EIS has been used to characterize Li plating

for a long time, most of the earlier studies were qualitative due to the difficulty of extracting the information on Li plating. Both Li plating and Li intercalation are Faradaic processes in the EIS test. They are a pair of competing reactions convoluted in the semicircle of the charge transfer process, leading to great difficulty to separate them.

Petzl et al. employed a low-temperature ($-22\text{ }^{\circ}\text{C}$) cycling aging study on commercial LFP batteries to cause Li plating, which was proven by post-mortem characterization.¹⁴³ The impedance evolution shows that the R_{SEI} and R_{ct} have hardly changed, while R_{ohm} increase slightly, owing to the electrolyte consumption caused by the reaction between plated lithium and electrolyte. Schuster et al. used EIS to investigate the nonlinear aging characteristics of LIBs, which found that Li plating could occur after a long-term duration at moderate working conditions and cause the knee point.¹⁴⁴ The increase of R_p in the midfrequency range is regarded as the signal of the occurrence of Li plating. However, it is hard to distinguish the information on Li plating from Li intercalation by ECM. EIS accompanied by DRT is more effective in this issue. Chen et al. used DRT to analyze the EIS of NMC cells cycled at normal and low temperature. As shown in Figure 9a, Li plating causes the shift of the R_{ct} peak to high frequency, accompanied by a decrease in peak intensity.¹⁴⁵ The results indicate that Li plating could lead to a rise of the time constant and a decrease of resistance of the charge-transfer process. Thus, the shift of the DRT peak of the charge-transfer process is considered as an indicator for the onset of Li plating. Gargh et al. used DRT to study the impedance change of NMC/graphite cells during fast charging,¹⁴⁶ which found that the impedance of batteries with Li plating significantly reduced after charging and then increased to the baseline value during the relaxation period. The authors ascribe the phenomenon to the damage of the SEI layer by Li plating and the reformation of SEI during the relaxation period, but it should relate to the Li plating on the anode and reintercalation during relaxation.

Combining voltage relaxation with EIS is an effective strategy to detect Li plating. It is known that the plated Li could undergo chemical transformation to intercalated Li during the relaxation process. Schindler et al. investigated the impedance change during the relaxation time by conducting an EIS test for every 10 min after plating.¹⁴⁷ As shown in Figure 9b, the R_{ct} gradually enhances with an increase in relaxation time, indicating that the plated Li reduces the anodic charge transfer resistance, while the reintercalation process of the plated Li during relaxation enhances it. Similarly, Xu et al. also used the voltage relaxation process by employing a transient relaxation process during charging to observe the change in iR drop.¹⁴⁸ The resistance R_i defined from the iR drop is used as an indicator for the onset of Li plating since it would drop suddenly once Li plating occurs (Figure 9c). Koleti et al. controlled the time of the transient relaxation process based on the frequency of charge transfer reaction, which was able to test 85% of the total change of voltage profile in 3 s.¹⁴⁹ The impedance at the chosen frequency is obtained by an intermittent charging procedure interrupted by a relaxation process for every 1% SOC. The point where the impedance significantly decreases during charging is considered as the onset of Li plating.

In addition to classical EIS, DEIS techniques show some potential in Li plating detection. NFRA is able to identify the information on Li plating in Y_3 harmonic spectroscopy. Harting et al. found that Y_3 showed a more significant enhance-

than Y_2 in the midfrequency range in the cells aged at $-10\text{ }^{\circ}\text{C}$, which was not observed in the cells aged at $25\text{ }^{\circ}\text{C}$.⁵⁴ The phenomenon is attributed to the Li plating on the anode. Due to the different sensitivity of higher harmonics to Li plating, the intensity changes of $Y_3:Y_2$ at 50 Hz is chosen as an indicator for Li plating, though the physical and quantitative relations between them are hard to build up. Koseoglou et al. employed continuous linear DEIS during the fast-charging procedure with a narrow frequency range (3.2 kHz to 1 Hz), short time (9 s), and small SOC variation (<1.5%) for each impedance test.¹⁵⁰ The *operando* impedance exhibits an abrupt decrease at high SOC, indicating the onset of Li plating. Brown et al. used linear DEIS and DRT to study the impedance change of Li plating during fast charging in three-electrode NMC cells.⁷³ Despite the decrease in R_{ct} , a significant increase in R_{SEI} is observed, as shown in Figure 9d. The inflection point is considered as the onset of Li plating. The plating detection method is cross-validated by *ex situ* mass titrations of Li metal, which proves to possess high Li detection sensitivity (<0.6% of the graphite capacity). Xu et al. developed an *operando* Li plating detection and quantification method based on single-frequency DEIS.¹⁵¹ Since Li plating causes a big enhancement of electrochemical active surface area (ECSA) so as to increase the electrochemical double layer capacitance (EDLC), the EDLC on the surface of graphite anode could be used as a quantitative indicator for Li plating. The characteristic frequency of the charge-transfer process of the graphite anode is first determined as 15 Hz and used in single-frequency DEIS to observe the dynamic capacitance variation during charging. As shown in Figure 9e, the capacitance of the graphite anode shows a significant linear rising tendency after charging to a point, which is regarded as the onset of Li plating. Moreover, a linear relationship between the amount of plated Li and capacitance evolution is constructed to achieve the quantitatively study about the inactive Li, which is further validated by TGC method. It is an innovative impedance-based method that not only detects the onset of Li plating but also quantifies the inactive Li, though there is still room for improvement in quantification capability on low-content plated Li.

In summary, the effects of Li plating on the electrochemical impedance (EIS) of the negative electrodes such as graphite electrodes can be summarized as follows: (1) exposing newly plated Li to the electrolyte leads to the growth of new SEI layer, accompanied with the rise of R_{SEI} ; (2) the resistance of charge transfer process should decrease, while the double layer capacitance would increase; (3) the time constant of the charge transfer process may change, corresponding to the shift of peak in DRT. Based on these characteristics, different impedance-based methods have been developed and are shown in Table 4. Generally, the impedance of the charge-transfer process consists of two different but tightly related and convoluted processes, Li intercalation and Li plating. Both of them are faradaic reactions with close time constants. Once Li plating occurs, the activation energy of Li deposition will remarkably decrease compared with the nucleation process, making it much easier to occur than intercalation in kinetic. Thus, the R_{ct} of Li plating is much smaller than that of Li intercalation. Based on the discussion, the change of peak intensity and time constant of charge transfer process in DRT should be attributed to variable dominance between the two processes. Nevertheless, the modeling of the anode's EIS after

Method	Required testing	Signal of Li plating	Mechanism	Onset condition	Ref
DCM	Single-frequency DEIS is used to monitor the change of "Z" at 15 Hz so as to monitor the capacitance change during charging process	The emergence of an upward trend of C_{dl} is considered as the onset of Li plating, with the normalized intensities used to quantified the amount of inactive Li	The onset of Li plating causes a rapid increase in ECSA and the rise in double layer capacitance consequently	✓	Operando and Quantification 151
NFRA	A high amplitude (1.5 C) alternating current is employed to obtain the higher harmonics	The rise of Y_3/Y_2 ratio at midfrequency range is considered as a signal of Li plating	The higher harmonics show different sensitivity to Li plating, while Y_3 increases more significantly than Y_2	✓	In situ 51
DEIS+DRT	The continuous DEIS is employed to monitor the R_{SEI} evolution during fast charging process	The emergence of an upward trend of R_{SEI} is considered as the onset of Li plating	When Li plating occurs, the plated Li would break the SEI layer and form new SEI, leading to a rise of R_{SEI} with SOC increasing	✓	Operando 73
EIS+DRT	Classical EIS combined with DRT is used to unravel the impedance change caused by Li plating	The decrease of R_{ct} of the anode and its shift in DRT is considered as the signal of Li plating	The changes of R_{ct} and its time constant reflect the transformation of charge transfer reaction from Li intercalation to plating	✓	In situ 145
DEIS	The continuous DEIS is utilized to monitor the evolution of midfrequency impedance during charging procedure	The emergence of a downward trend of R_{ct} is considered as the onset of Li plating	Li plating could decrease the R_{ct} of graphite anode	✓	Operando 150
Impedance estimation	Monitoring the change of impedance during voltage relaxation process with a specific relaxation time	The sudden decrease of the estimated impedance indicates the occurrence of Li plating	With a certain length of relaxation time, the estimated resistance could reflect the impedance of high and midfrequency range. The Li plating could decrease R_{ohm} and R_{ct}	✓	In situ 149
<i>iR</i> drop	Quantifying the impedance (R_i) based on the <i>iR</i> drop in the periodical transient relaxation during fast charging process	The emergence of a downward trend of R_i is considered as the onset of Li plating	The plated Li could decrease the R_{ohm} of graphite anode so as to cause the drop of R_i obtained from the transient state analysis	✓	In situ 148
VR+EIS	Classical EIS is applied continuously in parallel to the voltage relaxation process	The increase of R_{ohm} and R_{ct} during the voltage relaxation indicate the occurrence of Li plating	The chemical intercalation during the voltage relaxation decreases the amount of plated Li on graphite surface	×	In situ 147

Li plating and the quantification of plated Li by impedance with low detection limit are still big challenges.

4.2.2. SEI Formation and Growth. Since Peled put forward the formation of SEI on Li for the first time in 1979,¹⁵² SEI has drawn great attention and wide applications by battery researchers. It was proposed as an ionic conductive and electronic isolated passivation layer, which is formed on the surface of Li and the graphite anode once the anode contacts with electrolyte.¹⁵³ SEI plays a crucial role in determining the battery performance, as it could protect the anode and prevent it from further reacting with the electrolyte. Despite its positive effects, it could consume lithium inventory and electrolyte, impede the diffusion, and enhance the resistance of the electrodes. The continuous growth of the SEI is a main degradation mechanism in battery aging, when the thickness and resistance gradually increase in the process. EIS is one of the most powerful tools to characterize SEI due to its advantages of nondestructivity, *in situ* measurement, and easy accessibility.¹⁵⁴ The impedance and time constant of SEI could be easily obtained from EIS plot by ECM or DRT. At present, it has been commonly used to characterize SEI performance, evaluate novel electrolyte,¹⁵⁵ study SEI formation,^{156–158} and monitor SEI evolution.¹⁵⁹

As the growth of the SEI is one of the main degradation mechanisms of LIBs, the impedance change could reflect the evolution of the SEI during battery aging. Steinhauer et al. used *in situ* EIS and DRT methods to monitor the SEI formation process by carrying out EIS measurements at equidistant voltage intervals of 0.1 V during the first two cycles.¹⁶⁰ As shown in Figure 10a, the interfacial impedance showed a maximum in the voltage region between 0.8 and 0.3 V vs Li/Li⁺ in the first lithiation and decreased in the second lithiation, indicating that SEI completely formed in the first cycle. Qu et al. compared the impedance and DRT evolutions between two cells by using baseline electrolyte (1.0 M LiPF₆ in EC/EMC 3/7) and improved electrolyte (1.0 M LiPF₆ in EC/EMC/DMC 5/30/65 with 1% VC and 0.5% LiBOB) during 100 cycles at 60 °C.¹⁶¹ The cell with improved electrolyte shows a much smaller impedance rise and better cycling performance. The results are ascribed to a dense SEI layer, determined by comparing the CPE values of the initial EIS after formation cycle since low capacitance indicates low surface area and porosity. Moreover, the EIS and physical characterization coupled strategy play a vital role in relating SEI impedance to its composition. Wang et al. associated *in situ* EIS and DRT with XPS to study the formation and evolution of SEI, which found that the high-frequency and midfrequency semiarcs derived from the inorganic and organic components, respectively.¹⁵⁹ In Figure 10b, the resistance of organic layer first increases and then decreases, accompanying with the increase of the resistance of inorganic layer. The evolution indicates that organic components could transform to inorganic components in the first 50 cycles. The rupture-reformation mechanism is proposed to explain the increase of R_{SEI} . Xu et al. combined time-of-flight secondary ion mass spectroscopy (TOF-SIMS) with EIS to study the influence of dissolved Ni²⁺ on the composition, structure and impedance evolutions of SEI (Figure 10c).¹⁶²

The thickness of the SEI is supposed to be a good indicator for battery states during aging.¹⁶³ However, it is very hard to achieve an *in situ* observation on SEI, needless to say, through *in situ* monitoring the evolution of SEI thickness during aging. EIS seems to be a promising indirect method because it can

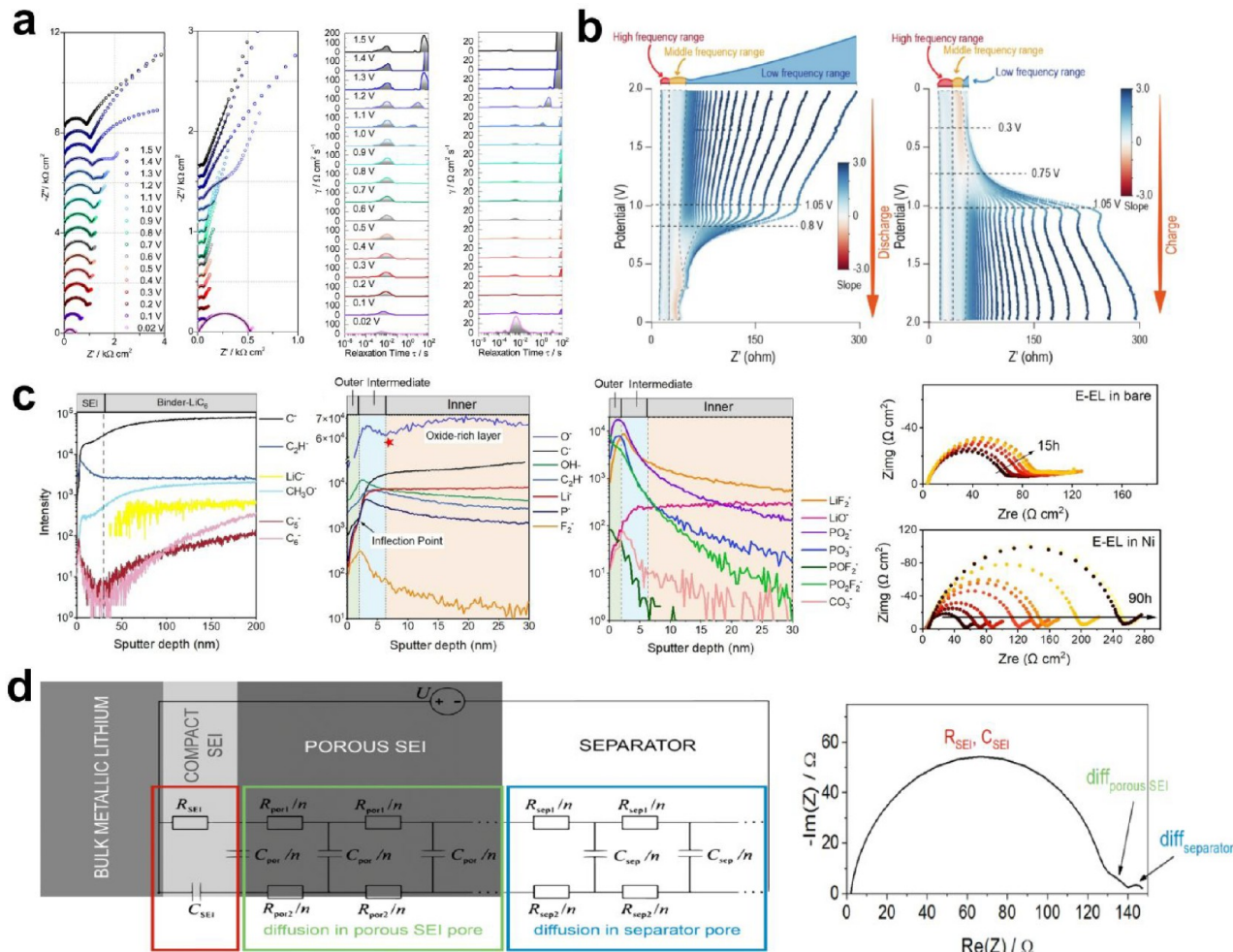


Figure 10. (a) EIS and corresponding DRT of a graphite anode during the first and second lithiation. Reprinted with permission from ref 160. Copyright 2017 Elsevier. (b) Differential Nyquist top diagram of the cell during the 50th cycle in cathodic and anodic processes. Reprinted with permission from ref 159. Copyright 2022 Elsevier. (c) TOF-SIMS depth profiles of selected secondary ion fragments on the surface of the E-EL electrode. The EIS profiles of electrodes stored in the pure electrolyte and the electrolyte with the addition of Ni^{2+} . Reprinted with permission from ref 162. Copyright 2022 John Wiley and Sons. (d) Transmission line model and typical corresponding impedance spectrum with denoted main processes. Reprinted with permission from ref 168. Copyright 2019 American Chemical Society.

obtain the resistance and capacitance of SEI nondestructively. Nevertheless, it is still a thorny issue to transfer its electrical property to thickness due to its inhomogeneous structure. If the structure of SEI is assumed to be homogeneous, and the ionic resistivity and dielectric permittivity are unvaried during aging, the SEI thickness (d_{SEI}) can be calculated based on the capacitance formula of plate capacitor and resistance formula shown in eqs 23 and 24, where ϵ_0 , ϵ_r , σ , and A represent permittivity of vacuum, relative permittivity, ionic conductivity, and surface area, respectively. However, the assumption apparently deviates from the realistic conditions. The impedance of SEI is determined not only by the thickness but also the chemical composition and morphology. Lu et al. found that the inorganic components were less capacitive and more conductive compared to organic species.¹⁵⁸ The impedance of inorganic components and organic components could be highly different due to their different structure, porosity, and dielectric constant. Hence, eq 23 needs to be rectified based on the SEI structure and growth law.

$$d_{\text{SEI}} = \frac{\epsilon_0 \epsilon_r A}{C_{\text{SEI}}} \quad (23)$$

$$d_{\text{SEI}} = R_{\text{SEI}} \sigma \quad (24)$$

SEI film is generally recognized as a complex structure consisting of an inner, thin, and compact layer close to the particle surface of about a few nanometers and an outer, thick, porous layer exposed to electrolyte. Based on this understanding, several physics-based models have been constructed to describe the relations between SEI growth and impedance variation. Ploehn et al. developed a diffusion-controlled model which predicts that SEI thickness increases linearly with the square root of time.¹⁶⁴ Safari et al. developed the porous SEI model to evaluate the effects of SEI porosity on capacity decay and interfacial resistance increase.¹⁶⁵ Chen et al. proposed a microstructure-aware impedance model to predict the effect of the electrode microstructure on SEI thickness and interfacial resistance.¹⁶⁶ Single et al. modeled the SEI as a porous surface film and developed a physics-based model based on a thermodynamically consistent theory for electrolyte transport.¹⁶⁷ The model introduced two parameters, porosity and tortuosity, to rectify the resistance formula in order to describe the porous SEI structure. Though the proposed analytical impedance expressions approximately are in accord with the

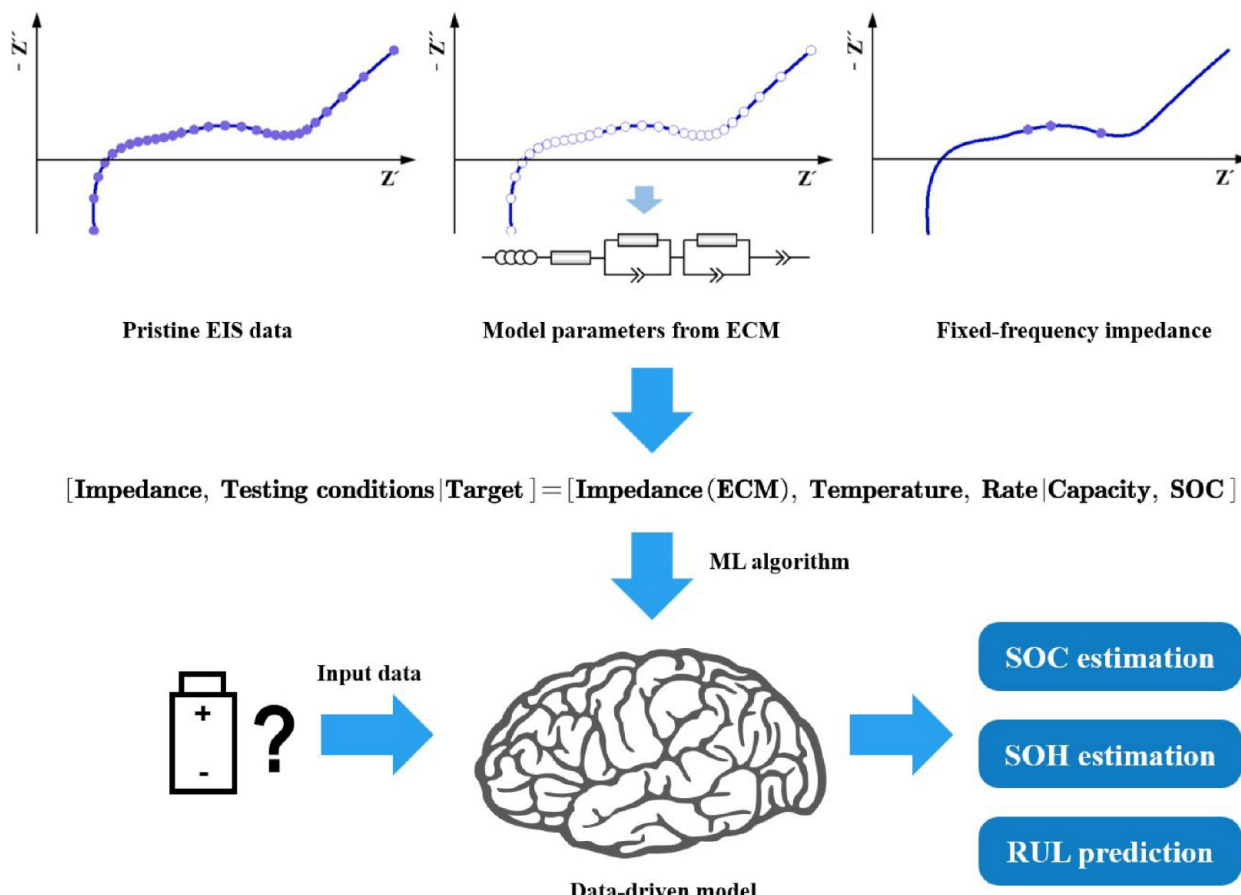


Figure 11. Three categories of feature extraction methods provide the data-driven sources for machine learning-based battery state prediction. Reprinted with permission from ref 180. Copyright 2022 Elsevier.

results of ECM, the model is overparametrized with experimentally inaccessible parameters. Tailian et al. built a SEI impedance model by using a RC-element and transmission line model to simulate the composite layer and porous layer, respectively (Figure 10d), which could achieve a good fitting effect for further quantitative analysis.¹⁶⁸ Recently, Santos et al. combined feedback and multifrequency alternating-current modes of scanning electrochemical microscopy (SECM) to evaluate quantitatively the local and *in situ* electronic and ionic properties of SEI in LIBs for the first time, respectively.¹⁶⁹ The method has potential in calculating the critical parameters of SEI, such as resistivity and dielectric permittivity.

In summary, although EIS is a proven technique in characterizing the electrical properties of SEI, the thorny issue is to quantitatively assess the thickness evolution of the SEI during battery aging by monitoring impedance change. To achieve this work, the resistivity and permittivity of individual SEI components or organic and inorganic layers are necessary parameters. Moreover, in-depth understanding of the structure and composition variation during SEI growth is required to build SEI models.

4.3. Machine Learning for Battery States Estimation. In recent years, machine learning (ML) has played a more and more instrumental role in LIBs and other energy storage applications.¹⁷¹ As EIS could reflect the internal information on LIBs and highly correlate with battery states, it could be used as the input data in machine learning to get data-driven models for SOC, SOH estimation, and RUL prediction. SOC, defined as the ratio of current capacity to nominal capacity, is

usually estimated by ampere hour counting and the OCV methods. However, the ampere hour counting method suffers from the problem of accumulating errors. The OCV method, although accurate, requires a long time, which is not suitable under working conditions. Since the impedance at specific frequency ranges are SOC dependent, it can also be used to estimate the SOC.¹⁷² In addition, as it is fairly difficult to measure the aging behavior under random accelerated conditions, constructing an impedance-based model for SOH estimation is of vital importance. Generally, the performance of data-driven models highly depends on the ML algorithms, quality, and quantity of data and feature extraction. The commonly used algorithms contain Gaussian process regression, support vector regression, random forest regression, deep neural networks, and so on. All of these methods have their advantages and disadvantages, as discussed more comprehensively elsewhere.^{173–175} This review mainly pays attention to different categories of initial data, feature extraction methods, and their effects on model performance.

There are usually three categories of feature extraction methods used in machine learning, i.e., the broadband EIS without any feature engineering, model parameter based on ECM, and single-frequency impedance feature (Figure 11). Zhang et al. used over 20000 impedance spectra of commercial LCO/graphite batteries at different operation conditions as the database and employed Gaussian process regression to predict RUL of batteries without knowing its past operating histories.²² The EIS spectra are directly taken as inputs. In this way, the spectral features used to predict degradation are

Table 5. Impedance-Based Data-Driven Models for SOH, SOC Estimation, and RUL Prediction

Battery chemistry	Experimental conditions	Pristine Data	Number of features	Feature extraction	ML method	Target	Error	Ref
45 mAh LCO	25, 35, 45 °C, 1C charge-2C discharge (1CC-2CD)	Collect EIS every even cycles	120 (Z' and Z'' of all frequency points)	Automatic	GRP	RUL	$R^2 = 0.88, 0.81, 0.72$ for 25, 35, 45 °C	22
				Automatic	DNN	RUL	0.60% MAPE	182
				Automatic	SVR-RBF	SOH	$R^2 = 0.92$	183
2.5 Ah LFP	25–60 °C, 5–100% SOC	Collect EIS every 10% SOC	4 (R_{ohm} , R_p , C_{dl} , R_w)	ECM (Manually)	ANN	SOC	1.2% RMSE	177
2 Ah NMC	1CC-1.5CD	Collect EIS every 200 cycles	4 (R_{ohm} , R_{SEL} , R_{ct} , terminal voltage)	ECM (Manually)	GA-BP	SOH	1.6% RMSE 1.7% MAPE	176
3.5 Ah NMC	25, 35, 45 °C, 0.5CC-1CD	Collect EIS every 50 cycles	4 (Z' and Z'' of 0.25 and 398 Hz)	Fix-frequency (Manually)	LR	SOH	1.0% RMSE	179
				SVM	SOH	0.64% RMSE		
				GRP	SOH	0.50% RMSE		
2.75 Ah NCA	25, 35 °C, 0.5CC-1CD, 0.5CC-NEDC	Collect EIS every 25 cycles	122 (Z' and Z'' of all frequency points) 5 (R_{ohm} , R_{SEL} , C_{SEL} , R_{ct} , C_{dl}) 6 (Z' and Z'' of 1, 5, and 10 Hz)	Automatic	GRP	SOH	1.2% RMSE 0.83% MSD	180
				ECM (Manually)	GRP	SOH	0.93% RMSE 0.80% MSD	
				Fix-frequency (Manually)	GRP	SOH	0.90% RMSE 0.67% MSD	

automatically determined, which shows the most predictive in the low-frequency region. However, directly using the whole EIS as input without artificially selecting features could lead to some problems. First, there are more than 100 input values for a single Nyquist plot. The huge amounts of data would lead to a long training time and low efficiency of the models. Moreover, the data quality could seriously influence feature selection and model accuracy since the features are completely based on the algorithm and raw EIS data. Thus, a great deal of EIS data are necessary to decrease the error caused by data quality.

Extracting the information inside EIS by ECM is a good approach to improve the accuracy and efficiency of the ML model, as the ECM could reflect the battery states with fewer parameters. Liu et al. used the second-order Randles circuit to fit EIS data, while the three as-obtained model parameters, R_{ohm} , R_{SEL} , and R_{ct} , were further used as inputs for neural network.¹⁷⁶ By conducting the genetic algorithm to optimize the back-propagation neural network, the training model could predict SOH based on the three ECM parameters, with both mean absolute error (MAE) and root-mean-square error (RMSE) near 1.6%. Moreover, it is found that the MAE rapidly increases to 4.8% when using the data with $\text{SOH} > 80\%$ as training data and $\text{SOH} < 80\%$ as testing data, indicating that the comprehensiveness and representativeness of the input data could markedly influence the model performance. Pizarro et al. also used four ECM-derived parameters as input data and SOC as target to build a model based on an artificial neural network, which achieved the SOC estimation with 1.2% RMSE.¹⁷⁷

Different from the ECM parameter-based feature, fix-frequency impedance-based feature is to select the impedance at a specific frequency that correlates tightly to capacity or SOC. The mechanism is similar to single-frequency DEIS. As the processes related to the degradation mechanism possess time constants, selecting the impedances at the corresponding frequency could reflect the effects of the degradation mechanism on capacity decay. Locorotondo et al. found that there may be a certain frequency point that can be considered as a reliable indicator of SOH through data clustering.¹⁷⁸ Zhu et al. first investigated the relations between battery capacity and impedance, which found that the impedance at two

frequencies (0.25 and 398 Hz) exhibited the highest correlation coefficient with the capacity fade.¹⁷⁹ Therefore, they used the real and imaginary part of the two single-frequency impedance, i.e., four parameters, as features combined with different machine learning algorithms, including linear regression (LR), support vector machine (SVM), and Gaussian process regression (GPR). The best model exhibited the lowest RMSE of 0.5% using the GPR algorithms. Jiang et al. conducted a comparative study of the three categories of representative features, including the broadband EIS feature, model parameter feature, and fixed-frequency impedance feature, with Gaussian process regression to figure out which type exhibits the best prediction performance.¹⁸⁰ It is found that the model using the proper fixed-frequency impedance as features showed the best estimation accuracy, efficiency, and confidence. The RMSE, mean standard deviation (MSD), and training time of single-frequency impedance model are 0.93%, 0.66%, 0.45 s, while the values of pristine EIS data-based model and ECM parameter-based model are 1.2%, 0.81%, 0.87 s and 0.93%, 0.80%, 0.45 s, respectively. Moreover, by choosing different parameter groups as inputs, a five parameters group, including R_{ohm} , R_{SEL} , C_{SEL} , R_{ct} , and C_{dl} shows a better model performance than the ten-parameters group containing all parameters of ECM and the three-parameters group containing resistance only. Nevertheless, the fixed-frequency impedances chosen in this contribution are 1, 5, and 10 Hz, whose positions are all located at the charge transfer process, leading to similar model performance when changing the combination of them. There is still room for improvement in the representativeness of the chosen frequency.

Besides only using impedance as inputs in the data-driven ML model, combining EIS with voltage profile and relevant differential curves may further improve the model accuracy. Li et al. integrated impedance data and charging data as basic data and conducted a cuckoo search algorithm to build up an online degradation diagnosis framework.¹⁸¹ By collecting the field data, the model can accurately identify eight parameters, where five parameters are impedance-related parameters and the others are the OCV-related parameters, including remaining capacity and stoichiometric parameters at the end of charge and end of discharge. The identified model parameters could

estimate both capacity decay and power decay with MAE values lower than 0.5% and 1.5%, respectively.

In summary, impedance-based models derived from ECM parameters and single-frequency impedance show better estimation performance, as the artificial selected features could reflect the battery states well. Table 5 concludes the existing studies that use impedance for SOC and SOH estimation. Nevertheless, some issues need to be considered. First, although a single-frequency impedance-based method exhibits the best estimation performance, it highly depends on the representativeness of the chosen frequencies on the specific degradation modes. Once the frequencies lose their representativeness, the error may become huge. Both the aging level and aging protocol of the batteries can also lead to a change of degradation mechanism and time constant variation. The operation conditions of aging protocols, such as charge/discharge rate and temperature, are rarely considered in the present ML models. Second, DRT has hardly been used for machine learning so far, owing to the considerable difficulty in data importing. Since it is a continuous function over time domain, how to filter the valuable data and discrete data from DRT is a thorny problem. Still, there is no doubt that DRT has huge potential in this application. Third, combining the voltage profile with impedance data for machine learning may achieve a better estimation performance. The voltage profile reflects the thermodynamic properties of electrode materials, while the EIS reflects the kinetic properties. The combination of them could act as the “fingerprint” of battery states. In addition, ORP-EIS is supposed to be a good method for SOC estimation since a continuous function of impedance to SOC could be obtained.

5. SUMMARY AND PERSPECTIVES

In summary, this review comprehensively introduces the principles, measurements, validation, modeling of EIS, and recent progress of its applications in LIBs' degradation and aging research. For classical EIS, the measurement should fulfill the linearity, stability, and causality conditions to guarantee the quality of the data. Since EIS modeling highly depends on the reliability of raw data, data validation by K-K relations should be a standard checkpoint before publication of impedance data. In addition, several typical dynamic EIS techniques are introduced, respectively. Furthermore, the commonly used modeling methods such as ECM, DRT, and TLM and their usage on general battery aging diagnosis are introduced and compared. Compared with the priori method ECM, DRT could be regarded as an upgraded substitute with a stronger quantitative ability to achieve degradation mechanism diagnosis, while TLM is a physics-based model that has a great advantage in analyzing porous electrodes and the influence of porosity variation on battery degradation.

The recent progress of EIS's application in LIB's degradation and aging research is summarized in three aspects. First, the EIS variations at different aging conditions of calendar aging and accelerated aging are systematically overviewed. EIS could not only diagnose the degradation mechanisms of LIBs at corresponding aging conditions, but it is also a good way to determine the boundary conditions of normal accelerated aging protocols for fast battery life test. Second, the newly developed impedance techniques in detecting Li plating and monitoring SEI growth, the two main degradation mechanisms, are elaborately reviewed. Several *Operando* DEIS techniques show great potential in detecting the onset of Li

plating in real-time battery working, among which R_{cv} , C_{dl} , and R_{SEI} could be considered as the indicators in different strategies. Lastly, an impedance-based data-driven model by machine learning for SOC, SOH estimation, and RUL prediction is introduced from the perspective of input data and feature extraction. The ECM parameters and fix-frequency impedance methods for feature extraction show better estimation performance of the models.

There are several challenging issues for developing advanced EIS techniques for *operando* estimation of the battery state and safety boundary, as listed below:

(1) Develop *operando* methods to detect Li plating with a low detection limit in the LIBs working at normal conditions. Currently, most of the reported methods detect the onset boundary of Li plating at low temperature, extremely fast charging, or overcharging, which possess a distinct and considerable amount of plated Li. However, if the plated Li is little and reversible, it will be difficult to detect it at the beginning stage of Li plating occurrence under normal operation conditions. Detection of residual Li plating during normal operation mode as early as possible and repair the state of LIBs is of vital practical importance. Moreover, non-destructively quantifying the amount of plated Li in the aged cells is also a challenging and meaningful task for safety issues.

(2) Achieve SEI thickness monitoring by *operando* EIS during battery work or aging research. EIS could extract the variations of the resistance and capacitance of SEI layer during battery aging. However, it is hard to build a robust relationship between the electric parameters and accurate SEI thickness. Sole use of EIS results is not sufficient for solving these tough issues. A combination of EIS and *in situ* physical characterization should be a necessary and promising way to bridge the contribution between the electric parameters and the thickness and composition of SEI layer, especially their dynamic relationships.

(3) Combine feature-extracted impedance data with the aging conditions to construct ML-based model for predicting battery aging behaviors, including cycling aging and calendar aging. Since battery aging conditions significantly influence the EIS evolutions, ML-models with these relations input could broaden the applicability of the model and reduce the experiments. Currently, ML is rarely used in calendar aging research. Considering the length of time needed in calendar aging studies, ML will be an indispensable tool in the future research. Moreover, how to introduce DRT results into ML-based model is also a challenge so as to realize a higher accuracy, since they contain more time-scale information than conventional methods.

(4) Develop credible *operando* EIS measuring methods for large-size batteries or battery pack. Although the reported impedance techniques are mature in small-size batteries for laboratory research, it is not easy to obtain comprehensive but *operando* EIS or onboard impedance spectrum of large-size batteries or even battery pack due to the cost limitation and technical difficulty. The impedance estimation methods still exhibit a relatively ambiguous accuracy, which require further improvements in measurement and algorithms.

(5) Develop efficient algorithms and fitting evaluation methods for DRT. Admittedly, DRT is a powerful tool for EIS modeling and in-depth mechanism research. However, the existence of artificial parameters and flexibility of modeling process could cause errors and misunderstandings in the vertical comparison of battery aging research. Thus, it is urgent

to improve the algorithms and develop a better fitting program, even a “one-click” fitting program without artificial parameters, to achieve higher accuracy and efficiency.

Anyway, although EIS could provide abundant information about battery states such as State of Charge (SOC) or State of Health (SOH) during battery aging, as EIS is mostly electrical-based data which is not difficult to be deconvoluted using a simple equivalent circuit model, it is necessary to combine EIS with other physical and electrochemical characterization methods to calibrate the data quantitatively and obtain a cross-validated conclusion rather than using EIS alone. We expect that EIS could push and contribute our understanding and insight into battery aging behavior to a deeper level once these problems are worked out.

■ AUTHOR INFORMATION

Corresponding Author

Yong Yang — *State Key Laboratory for Physical Chemistry of Solid Surfaces, Collaborative Innovation Center of Chemistry for Energy Materials and Department of Chemistry, College of Chemistry and Chemical Engineering and School of Energy, Xiamen University, Xiamen 361005, People's Republic of China; [ORCID: 0000-0002-9928-7165](https://orcid.org/0000-0002-9928-7165); Email: yyang@xmu.edu.cn*

Authors

Wenxuan Hu — *State Key Laboratory for Physical Chemistry of Solid Surfaces, Collaborative Innovation Center of Chemistry for Energy Materials and Department of Chemistry, College of Chemistry and Chemical Engineering, Xiamen University, Xiamen 361005, People's Republic of China; [ORCID: 0000-0003-1222-459X](https://orcid.org/0000-0003-1222-459X)*

Yufan Peng — *State Key Laboratory for Physical Chemistry of Solid Surfaces, Collaborative Innovation Center of Chemistry for Energy Materials and Department of Chemistry, College of Chemistry and Chemical Engineering, Xiamen University, Xiamen 361005, People's Republic of China*

Yimin Wei — *Contemporary Amperex Technology Co., Ltd., Ningde 352100, China*

Complete contact information is available at:

<https://pubs.acs.org/10.1021/acs.jpcc.3c00033>

Notes

The authors declare no competing financial interest.

■ ACKNOWLEDGMENTS

This research was financially supported by the National Key R&D Program of China (Grant No. 2021YFB2401800).

■ NOMENCLATURE

ANN	Artificial neural network
CPE	Constant phase element
CNLS	Complex nonlinear least-squares
CEI	Cathode electrolyte interface
CL	Conductivity loss
C_{SEI} (F)	Capacitance of SEI layer
C_{dl} (F)	Electric double-layer capacitance
d_{SEI} (nm)	Thickness of SEI layer
DRT	Distribution of relaxation times
DEIS	Dynamic electrochemical impedance spectroscopy
DNN	Deep neural network
DCM	Dynamic capacitance measurement

D-M-D	Dissolution-membrane-deposition
EIS	Electrochemical impedance spectroscopy
ECM	Equivalent circuit model
f (Hz)	Frequency
GPR	Gaussian process regression
Gr	Graphite
LCO	$LiCoO_2$
LFP	$LiFePO_4$
LR	Linear regression
LLI	Loss of lithium inventory
LAM	Loss of active materials
LTV	Linear time-varying
ML	Machine learning
MAE	Mean absolute error
MSD	Mean standard deviation
NLTVA	Nonlinear time-varying
NFRA	Nonlinear frequency response analysis
NMC	$LiNi_xCo_yMn_zO_2$
NCA	$LiNi_xCo_yAl_zO_2$
ORP-EIS	Odd random phase electrochemical impedance spectroscopy
RT	Room temperature
RUL	Remaining useful life
RMSE	Root means square error
R_{ohm} (Ω)	Ohmic resistance
R_{SEI} (Ω)	Ion diffusion resistance of SEI layer
R_{ct} (Ω)	Charge transfer resistance
R_{ion} (Ω)	Ion diffusion resistance in pores
R_W (Ω)	Warburg resistance
R_p (Ω)	Polarization resistance; the real part of impedance between the R_{ohm} and R_W
SVM	Support vector machine
SEI	Solid electrolyte interface
SOC	State of charge
SOH	State of health
TLM	Transmission line model
TM	Transition metal
Y_n	n -th harmonic ($n = 2, 3, 4\dots$)
Z' (Ω)	Impedance of real part
Z'' (Ω)	Impedance of imaginary part
τ (s)	Time constant

■ REFERENCES

- (1) Palacin, M. R.; de Guibert, A. Why do batteries fail? *Science* **2016**, *351* (6273), 1253292.
- (2) Li, W.; Li, M.; Hu, Y.; Lu, J.; Lushington, A.; Li, R.; Wu, T.; Sham, W. K.; Sun, X. Synchrotron-Based X-ray Absorption Fine Structures, X-ray Diffraction, and X-ray Microscopy Techniques Applied in the Study of Lithium Secondary Batteries. *Small Methods* **2018**, *2*, 1700341.
- (3) Han, B.; Zou, Y. C.; Xu, G. Y.; Hu, S. G.; Kang, Y. Y.; Qian, Y. X.; Wu, J.; Ma, X. M.; Yao, J. Q.; Li, T. T.; et al. Additive Stabilization of SEI on Graphite Observed Using Cryo-Electron Microscopy. *Energy Environ. Sci.* **2021**, *14*, 4882–4889.
- (4) Fang, C.; Li, J.; Zhang, M.; Zhang, Y.; Yang, F.; Lee, J. Z.; Lee, M. H.; Alvarado, J.; Schroeder, M. A.; Yang, Y.; et al. Quantifying inactive lithium in lithium metal batteries. *Nature* **2019**, *572*, 511–515.
- (5) Tao, M.; Xiang, Y.; Zhao, D.; Shan, P.; Sun, Y.; Yang, Y. Quantifying the Evolution of Inactive Li/Lithium Hydride and Their Correlations in Rechargeable Anode-free Li Batteries. *Nano Lett.* **2022**, *22* (16), 6775–6781.
- (6) Tao, M.; Xiang, Y.; Zhao, D.; Shan, P.; Yang, Y. Protocol for quantifying inactive lithium in anode-free lithium batteries by mass spectrometry titration. *Commun. Mater.* **2022**, *3*, 50.

- (7) Xiang, Y.; Tao, M.; Zhong, G.; Liang, Z.; Zheng, G.; Huang, X.; Liu, X.; Jin, Y.; Xu, N.; Armand, M.; et al. Quantitatively analyzing the failure processes of rechargeable Li metal batteries. *Sci. Adv.* **2021**, *7*, eabj3423.
- (8) Wandt, J.; Jakes, P.; Granwehr, J.; Eichel, R. A.; Gasteiger, H. A. Quantitative and Time-resolved Detection of Lithium Plating on Graphite Anodes in Lithium Ion Batteries. *Mater. Today* **2018**, *21*, 231–240.
- (9) Chen, X.; Hu, Y.; Li, S.; Wang, Y. X.; Li, D.; Luo, C.; Xue, X.; Xu, F.; Zhang, Z.; Gong, Z. L.; et al. State of Health (SoH) Estimation and Degradation Modes Analysis of Pouch NMC532/Graphite Li-ion Battery. *J. Power Sources* **2021**, *498*, 229884.
- (10) Campbell, I. D.; Marzook, M.; Monica, M.; Offer, G. J. How Observable Is Lithium Plating? Differential Voltage Analysis to Identify and Quantify Lithium Plating Following Fast Charging of Cold Lithium-Ion Batteries. *J. Electrochem. Soc.* **2019**, *166* (4), 725–739.
- (11) Adam, A.; Knobbe, E.; Wandt, J.; Kwade, A. Application of the Differential Charging Voltage Analysis to Determine the Onset of Lithium-plating During Fast Charging of Lithium-ion Cells. *J. Power Sources* **2021**, *495*, 229794.
- (12) He, J.; Bian, X.; Liu, L.; Wei, Z.; Yan, F. Comparative study of curve determination methods for incremental capacity analysis and state of health estimation of lithium-ion battery. *J. Energy Storage* **2020**, *29*, 101400.
- (13) Smith, A. J.; Burns, J. C.; Trussler, S.; Dahn, J. R. Precision Measurements of the Coulombic Efficiency of Lithium-ion Batteries and of Electrode Materials for Lithium-ion Batteries. *J. Electrochem. Soc.* **2010**, *157*, 196–202.
- (14) Burns, J. C.; Stevens, D. A.; Dahn, J. R. In-situ Detection of Lithium Plating Using High Precision Coulometry. *J. Electrochem. Soc.* **2015**, *162*, 959–964.
- (15) Gaberšček, M. Understanding Li-based battery materials via electrochemical impedance spectroscopy. *Nat. Commun.* **2021**, *12*, 6513.
- (16) Hahn, M.; Schindler, S.; Triebs, J. C.; Danzer, M. A. Optimized process parameters for a reproducible distribution of relaxation times analysis of electrochemical systems. *Batteries* **2019**, *5*, 43.
- (17) Schönleber, M.; Ivers-Tiffée, E. The Distribution Function of Differential Capacity as a new tool for analyzing the capacitive properties of Lithium-Ion batteries. *Electrochim. Commun.* **2015**, *61*, 45–48.
- (18) Quattrocchi, E.; Wan, T. H.; Curcio, A.; Pepe, S.; Effat, M. B.; Ciucci, F. A general model for the impedance of batteries and supercapacitors: The non-linear distribution of diffusion times. *Electrochim. Acta* **2019**, *324*, 134853.
- (19) Lyu, N.; Jin, Y.; Xiong, R.; Miao, S.; Gao, J. Real-time overcharge warning and early thermal runaway prediction of Li-ion battery by online impedance measurement. *IEEE Trans. Ind. Electron.* **2022**, *69* (2), 1929–1936.
- (20) Iurilli, P.; Brivio, C.; Wood, V. On the use of electrochemical impedance spectroscopy to characterize and model the aging phenomena of lithium-ion batteries: a critical review. *J. Power Sources* **2021**, *505*, 229860.
- (21) Qu, D.; Wang, G.; Kafle, J.; Harris, J.; Crain, L.; Jin, Z.; Zheng, D. Electrochemical Impedance and its Applications in Energy-Storage Systems. *Small Methods* **2018**, *2*, 1700342.
- (22) Zhang, Y.; Tang, Q.; Zhang, Y.; Wang, J.; Stimming, U.; Lee, A. Identifying degradation patterns of lithium ion batteries from impedance spectroscopy using machine learning. *Nat. Commun.* **2020**, *11*, 1706.
- (23) Wang, S.; Zhang, J.; Gharbi, O.; Vivier, V.; Gao, M.; Orazem, M. E. Electrochemical impedance spectroscopy. *Nat. Rev. Methods Primers* **2021**, *1*, 41.
- (24) Vivier, V.; Orazem, M. E. Impedance Analysis of electrochemical system. *Chem. Rev.* **2022**, *122*, 11131–11168.
- (25) Ciucci, F. Modeling electrochemical impedance spectroscopy. *Curr. Opin. Electrochem.* **2019**, *13*, 132–139.
- (26) Lu, Y.; Zhao, C.; Huang, J.; Zhang, Q. The Timescale Identification Decoupling Complicated Kinetic Processes in Lithium Batteries. *Joule* **2022**, *6*, 1172–1198.
- (27) Gaddam, R. R.; Katzenmeier, L.; Lamprecht, X.; Bandarenka, A. S. Review on physical impedance models in modern battery research. *Phys. Chem. Chem. Phys.* **2021**, *23*, 12926–12944.
- (28) McCarthy, K.; Gullapalli, H.; Ryan, K. M.; Kennedy, T. Review—Use of Impedance Spectroscopy for the Estimation of Li-ion Battery State of Charge, State of Health and Internal Temperature. *J. Electrochem. Soc.* **2021**, *168*, No. 080517.
- (29) Wang, X.; Wei, X.; Zhu, J.; Dai, H.; Zheng, Y.; Xu, X.; Chen, Q. A Review of Modeling, Acquisition, and Application of Lithium-Ion Battery Impedance for Onboard Battery Management. *eTransportation* **2021**, *7*, 100093.
- (30) Osaka, T.; Mukoyama, D.; Nara, H. Review—Development of Diagnostic Process for Commercially Available Batteries, Especially Lithium Ion Battery, by Electrochemical Impedance Spectroscopy. *J. Electrochem. Soc.* **2015**, *162* (14), 2529–2537.
- (31) Meddings, N.; Heinrich, M.; Overney, F.; Lee, J. S.; Ruiz, V.; Napolitano, E.; Seitz, S.; Hinds, G.; Racchichini, R.; Gaberšček, M.; et al. Application of electrochemical impedance spectroscopy to commercial Li-ion cells: A review. *J. Power Sources* **2020**, *480*, 228742.
- (32) Hirschorn, B.; Tribollet, B.; Orazem, M. E. On Selection of the Perturbation Amplitude Required to Avoid Nonlinear Effects in Impedance Measurements. *Isr. J. Chem.* **2008**, *48*, 133–142.
- (33) Esteban, J. M.; Orazem, M. E. On the Application of the Kramers-Kronig Relations to Evaluate the Consistency of Electrochemical Impedance Data. *J. Electrochem. Soc.* **1991**, *138*, 67–76.
- (34) Schonleber, M.; Klotz, D.; Ivers-Tiffée, E. A Method for Improving the Robustness of linear Kramers-Kronig Validity Tests. *Electrochim. Acta* **2014**, *131*, 20–27.
- (35) Hahn, M.; Schindler, S.; Triebs, L. C.; Danzer, M. A. Optimized Process Parameters for a Reproducible Distribution of Relaxation Times Analysis of Electrochemical Systems. *Batteries* **2019**, *5*, 5.
- (36) Battistel, A.; La Mantia, F. On the Physical Definition of Dynamic Impedance: How to Design an Optimal Strategy for Data Extraction. *Electrochim. Acta* **2019**, *304*, 513–520.
- (37) Itagaki, M.; Kobari, N.; Yotsuda, S.; Watanabe, K.; Kinoshita, S.; Ue, M. *In situ* electrochemical impedance spectroscopy to investigate negative electrode of lithium-ion rechargeable batteries. *J. Power Sources* **2004**, *135*, 255–261.
- (38) Itagaki, M.; Kobari, N.; Yotsuda, S.; Watanabe, K.; Kinoshita, S.; Ue, M. LiCoO₂ electrode/electrolyte interface of Li-ion rechargeable batteries investigated by *in situ* electrochemical impedance spectroscopy. *J. Power Sources* **2005**, *148*, 78–84.
- (39) Huang, J.; Zhang, J. B.; Li, Z.; Song, S. L.; Wu, N. N. Exploring Differences between Charge and Discharge of LiMn₂O₄/Li Half-cell with Dynamic Electrochemical Impedance Spectroscopy. *Electrochim. Acta* **2014**, *131*, 228–235.
- (40) Itagaki, M.; Honda, K.; Hoshi, Y.; Shitanda, I. In-situ EIS to Determine Impedance Spectra of Lithium-Ion Rechargeable Batteries During Charge and Discharge Cycle. *J. Electroanal. Chem.* **2015**, *737*, 78–84.
- (41) Huang, J.; Ge, H.; Li, Z.; Zhang, J. B. Dynamic Electrochemical Impedance Spectroscopy of a Three-Electrode Lithium-Ion Battery during Pulse Charge and Discharge. *Electrochim. Acta* **2015**, *176*, 311–320.
- (42) Watanabe, H.; Omoto, S.; Hoshi, Y.; Shitanda, I.; Itagaki, M. Electrochemical Impedance Analysis on Positive Electrode in Lithium-Ion Battery with Galvanostatic Control. *J. Power Sources* **2021**, *507*, 230258.
- (43) Huang, J.; Li, Z.; Zhang, J. Dynamic electrochemical impedance spectroscopy reconstructed from continuous impedance measurement of single frequency during charging/discharging. *J. Power Sources* **2015**, *273*, 1098–1102.
- (44) Pintelon, R.; Louarroudi, E.; Lataire, J. Detecting and Quantifying the Nonlinear and Time-Variant Effects in FRF Measurements Using Periodic Excitations. *IEEE Trans. Instrum. Meas.* **2013**, *62* (12), 3361–3373.

- (45) Fasmin, F.; Srinivasan, R. Review—Nonlinear Electrochemical Impedance Spectroscopy. *J. Electrochim. Soc.* **2017**, *164* (7), 443–455.
- (46) Wilson, J. R.; Schwartz, D. T.; Alder, S. B. Nonlinear Electrochemical Impedance Spectroscopy for Solid Oxide Fuel Cell Cathode Materials. *Electrochim. Acta* **2006**, *51*, 1389–1402.
- (47) Koster, D.; Du, G. Q.; Battistel, A.; Mantia, F. L. Dynamic Impedance Spectroscopy Using Dynamic Multi-Frequency Analysis: A Theoretical and Experimental Investigation. *Electrochim. Acta* **2017**, *246*, 553–563.
- (48) Erinnwingbovo, C.; Siller, V.; Nunez, M.; Trocolo, R.; Brogioli, D.; Morata, A.; Mantia, D. L. Dynamic Impedance Spectroscopy of LiMn₂O₄ Thin Films Made by Multi-Layer Pulsed Laser Deposition. *Electrochim. Acta* **2020**, *331*, 135385.
- (49) Sacci, R. L.; Seland, F.; Harrington, D. A. Dynamic Electrochemical Impedance Spectroscopy for Electrocatalytic Reactions. *Electrochim. Acta* **2014**, *131*, 13–19.
- (50) Harting, N.; Wolff, N.; Roder, F.; Krewer, U. Nonlinear Frequency Response Analysis (NFRA) of Lithium-Ion Batteries. *Electrochim. Acta* **2017**, *248*, 133–139.
- (51) Harting, N.; Wolff, N.; Krewer, U. Identification of Lithium Plating in Lithium-Ion Batteries using Nonlinear Frequency Response Analysis (NFRA). *Electrochim. Acta* **2018**, *281*, 378–385.
- (52) Wolff, N.; Harting, N.; Heinrich, M.; Krewer, U. Nonlinear frequency response analysis on lithium-ion batteries: Process identification and differences between transient and steady-state behavior. *Electrochim. Acta* **2018**, *260*, 614–622.
- (53) Harting, N.; Wolff, N.; Roder, F.; Krewer, U. State-of-Health Diagnosis of Lithium-Ion Batteries Using Nonlinear Frequency Response Analysis. *J. Electrochim. Soc.* **2019**, *166* (2), 277–285.
- (54) Harting, N.; Schenkendorf, R.; Wolff, N.; Krewer, U. State-of-Health Identification of Lithium-Ion Batteries Based on Nonlinear Frequency Response Analysis: First Steps with Machine Learning. *Appl. Sci.* **2018**, *8*, 821.
- (55) Murbach, M. D.; Hu, V. W.; Schwartz, D. T. Nonlinear Electrochemical Impedance Spectroscopy of Lithium-Ion Batteries: Experimental Approach, Analysis, and Initial Findings. *J. Electrochim. Soc.* **2018**, *165* (11), 2758–2765.
- (56) Murbach, M. D.; Schwartz, D. T. Extending Newman's Pseudo-Two-Dimensional Lithium-Ion Battery Impedance Simulation Approach to Include the Nonlinear Harmonic Response. *J. Electrochim. Soc.* **2017**, *164* (11), 3311–3320.
- (57) Liebhart, B.; Satzke, M.; Komsiyska, L.; Endisch, C. Application of Nonlinear Impedance Spectroscopy for the Diagnosis of Lithium-Ion Battery Cells under Various Operating Conditions. *J. Power Sources* **2020**, *480*, 228673.
- (58) Van Gheem, E. V.; Pintelon, R.; Vereecken, J.; Schoukens, J.; Hubin, A.; Verboven, P.; Blajiev, O. Electrochemical impedance spectroscopy in the presence of non-linear distortions and non-stationary behaviour. *Electrochim. Acta* **2004**, *49* (26), 4753–4762.
- (59) Halleman, N.; Pintelon, R.; Zhu, X.; Collet, T.; Claessens, R.; Wouters, B.; Hubin, A.; Lataire, J. Detection, Classification, and Quantification of Nonlinear Distortions in Time-Varying Frequency Response Function Measurements. *IEEE Trans. Instrum. Meas.* **2021**, *70*, 6500814.
- (60) Halleman, N.; Pintelon, R.; Gheem, E. V.; Collet, T.; Claessens, R.; Wouters, B.; Ramharter, K.; Hubin, A.; Lataire, J. Best Linear Time-Varying Approximation of a General Class of Nonlinear Time-Varying Systems. *IEEE Trans. Instrum. Meas.* **2021**, *70*, 6503814.
- (61) Halleman, N.; Pintelon, R.; Zhu, X.; Collet, T.; Havigh, M. D.; Wouters, B.; Revilla, R. I.; Claessens, R.; Ramharter, K.; Hubin, A.; Lataire, J. Trend Removal in Measurements of Best Linear Time-Varying Approximations – with Application to *Operando* Electrochemical Impedance Spectroscopy. *IEEE Trans. Instrum. Meas.* **2022**, *71*, 6501711.
- (62) Zhu, X. H.; Halleman, N.; Wouters, B.; Claessens, R.; Lataire, J.; Hubin, A. *Operando* Odd Random Phase Electrochemical Impedance Spectroscopy as a Promising Tool for Monitoring Lithium-Ion Batteries during Fast Charging. *J. Power Sources* **2022**, *544*, 231852.
- (63) Halleman, N.; Widanage, W. D.; Zhu, X. H.; Moharana, S.; Rashid, M.; Hubin, A.; Lataire, J. *Operando* Electrochemical Impedance Spectroscopy and its Application to Commercial Li-Ion Batteries. *J. Power Sources* **2022**, *547*, 232005.
- (64) Gabersček, M. Impedance spectroscopy of battery cells: Theory versus experiment. *Curr. Opin. Electrochim.* **2022**, *32*, 100917.
- (65) Edge, J. S.; O'kane, S.; Prosser, R.; Kirkaldy, N. D.; Patel, A. N.; Hales, A.; Ghosh, A.; Ai, W. L.; Chen, J. Y.; Yang, J.; et al. Lithium Ion Battery Degradation: What You Need to Know. *Phys. Chem. Chem. Phys.* **2021**, *23*, 8200–8221.
- (66) O'Kane, S.; Ai, W. L.; Madabattula, G.; Alonso, D. A.; Timms, R.; Sulzer, V.; Edge, J. S.; Wu, B.; Offer, G. J.; Marinescu, M. Lithium-Ion Battery Degradation: How to Model it. *Phys. Chem. Chem. Phys.* **2022**, *24*, 7909–7922.
- (67) Jorcin, J. B.; Orazem, M. E.; Pebere, N.; Tribollet, B. CPE Analysis by Local Electrochemical Impedance Spectroscopy. *Electrochim. Acta* **2006**, *51*, 1473–1479.
- (68) Van Havenbergh, K.; Turner, S.; Driesen, K.; Bridel, J.-S.; Van Tendeloo, G. Solid-Electrolyte Interphase Evolution of Carbon-Coated Silicon Nanoparticles for Lithium-Ion Batteries Monitored by Transmission Electron Microscopy and Impedance Spectroscopy. *Energy Technol.* **2015**, *3*, 699–708.
- (69) Pastor-Fernández, C.; Uddin, K.; Chouchelamane, G. H.; Widanage, W. D.; Marco, J. A Comparison between Electrochemical Impedance Spectroscopy and Incremental Capacity-Differential Voltage as Li-ion Diagnostic Techniques to Identify and Quantify the Effects of Degradation Modes within Battery Management Systems. *J. Power. Sources* **2017**, *360*, 301–318.
- (70) Xiong, R.; Pan, Y.; Shen, W.; Li, H.; Sun, F. Lithium-ion battery aging mechanisms and diagnosis method for automotive applications: Recent advances and perspectives. *Renew. Sustain. Energy Rev.* **2020**, *131*, 110048.
- (71) Teliz, E.; Zinola, C. F.; Diaz, V. Identification and Quantification of Aging Mechanisms in Li-ion Batteries by Electrochemical Impedance Spectroscopy. *Electrochim. Acta* **2022**, *426*, 140801.
- (72) Xu, H. Y.; Han, C.; Li, W. T.; Li, H. Y.; Qiu, X. P. Quantification of Lithium Dendrite and Solid Electrolyte Interphase (SEI) in Lithium-Ion Batteries. *J. Power Sources* **2022**, *529*, 231219.
- (73) Brown, D. E.; McShane, E. J.; Konz, Z. M.; Knudsen, K. B.; McCloskey, B. D. Detecting Onset of Lithium Plating During Fast Charging of Li-ion Batteries Using *Operando* Electrochemical Impedance Spectroscopy. *Cell Rep. Phys. Sci.* **2021**, *2*, 100589.
- (74) Boukamp, B. A. Distribution (Function) of Relaxation Times, Successor to Complex Nonlinear Least Squares Analysis of Electrochemical Impedance Spectroscopy? *J. Phys. Energy* **2020**, *2*, No. 042001.
- (75) Tuncer, E.; Gubanski, S. M. Using the Monte Carlo Method to Obtain Relaxation Time Distribution and Comparing Non-linear Spectral Function Fits. *IEEE Trans. Dielectr. Electr. Insul.* **2001**, *8* (3), 310–320.
- (76) Boukamp, B. A. Fourier Transform Distribution Function of Relaxation Times; Application and Limitations. *Electrochim. Acta* **2015**, *154*, 35–46.
- (77) Tesler, A. B.; Lewin, D. R.; Baltianski, S.; Tsur, Y. Analyzing Results of Impedance Spectroscopy Using Novel Evolutionary Programming Techniques. *J. Electroceramics* **2010**, *24* (4), 245–260.
- (78) Hershkovitz, S.; Tomer, S.; Baltianski, S.; Tsur, Y. ISGP: Impedance spectroscopy analysis using evolutionary programming procedure. *ECS Trans.* **2011**, *33* (40), 67–73.
- (79) Saccoccio, M.; Wan, T. H.; Chen, C.; Ciucci, F. Optimal Regularization in Distribution of Relaxation Times Applied to Electrochemical Impedance Spectroscopy: Ridge and Lasso Regression Methods - A Theoretical and Experimental Study. *Electrochim. Acta* **2014**, *147*, 470–482.
- (80) Wan, T.; Saccoccio, M.; Chen, C.; Ciucci, F. Influence of the Discretization Methods on the Distribution of Relaxation Times

- Deconvolution: Implementing Radial Basis Functions with DRTtools. *Electrochim. Acta* **2015**, *184*, 483–499.
- (81) Quattrocchi, E.; Wan, T.; Belotti, A.; Kim, D.; Pepe, S.; Kalinin, S. V.; Ahmadi, M.; Ciucci, F. The deep-DRT: A deep neural network approach to deconvolve the distribution of relaxation times from multidimensional electrochemical impedance spectroscopy data. *Electrochim. Acta* **2021**, *392*, 139010.
- (82) Quattrocchi, E.; Py, B.; Maradesa, A.; Meyer, Q.; Zhao, C.; Ciucci, F. Deconvolution of Electrochemical Impedance Spectroscopy Data Using the Deep-Neural-Network-Enhanced Distribution of Relaxation Times. *Electrochim. Acta* **2023**, *439*, 141499.
- (83) Liu, J.; Ciucci, F. The Gaussian process distribution of relaxation times: A machine learning tool for the analysis and prediction of electrochemical impedance spectroscopy data. *Electrochim. Acta* **2020**, *331*, 135316.
- (84) Maradesa, A.; Py, B.; Quattrocchi, E.; Ciucci, F. The probabilistic deconvolution of the distribution of relaxation times with finite Gaussian processes. *Electrochim. Acta* **2022**, *413*, 140119.
- (85) Wang, J.; Huang, Q.; Li, W.; Wang, J.; Zhuang, Q.; Zhang, J. Fundamentals of distribution of relaxation times for electrochemical impedance spectroscopy. *J. Electrochem.* **2020**, *26* (5), 607–627.
- (86) Paul, T.; Chi, P.; Wu, P.; Wu, M. Computation of Distribution of Relaxation Times by Tikhonov Regularization for Li Ion Batteries: Usage of L-Curve Method. *Sci. Rep.* **2021**, *11*, 12624.
- (87) Zhu, D.; Ma, T. C.; Yang, Y. B. Optimization and Application of the Distribution of Relaxation Times Based on Characteristic Frequency Resolution and Hyperparameters. *J. Power Sources* **2022**, *545*, 231955.
- (88) Wang, C. L.; Zhu, G. Y.; Zhang, P. B.; Fang, X. H. Optimization Procedures for the Inversion of Impedance Spectra to the Distribution of Relaxation Times. *J. Electroanal. Chem.* **2022**, *911*, 116199.
- (89) Zic, M.; Pereverzyev, S.; Subotic, V.; Pereverzyev, S. Adaptive Multiparameter Regularization Approach to Construct the Distribution Function of Relaxation Times. *GEM-Int. J. Geomath.* **2020**, *11* (1), 2.
- (90) Iurilli, P.; Brivio, C.; Wood, V. Detection of Lithium-Ion Cells' Degradation through Deconvolution of Electrochemical Impedance Spectroscopy with Distribution of Relaxation Time. *Energy Technol.* **2022**, *10*, 2200547.
- (91) Momma, T.; Yokoshima, T.; Nara, H.; Gima, Y.; Osaka, T. Distinction of impedance responses of Li-ion batteries for individual electrodes using symmetric cells. *Electrochim. Acta* **2014**, *131*, 195–201.
- (92) Gordon, I. J.; Genies, S.; Larbi, G. S.; Boulineau, A.; Daniel, L.; Alias, M. Original implementation of Electrochemical Impedance Spectroscopy (EIS) in symmetric cells: Evaluation of post-mortem protocols applied to characterize electrode materials for Li-ion batteries. *J. Power Sources* **2016**, *307*, 788–795.
- (93) Schmidt, J. P.; Chrobak, T.; Ender, M.; Illig, J.; Klotz, D.; Ivers-Tiffée, E. Studies on LiFePO₄ as cathode material using impedance spectroscopy. *J. Power Sources* **2011**, *196*, 5342–5348.
- (94) Xiao, Y.; Xu, R.; Yan, C.; Huang, J. Q.; Zhang, Q.; Ouyang, M. G. A Toolbox of Reference Electrodes for Lithium Batteries. *Adv. Funct. Mater.* **2022**, *32*, 2108449.
- (95) Hoshi, Y.; Narita, Y.; Honda, K.; Ohtaki, T.; Shitanda, I.; Itagaki, M. Optimization of reference electrode position in a three-electrode cell for impedance measurements in lithium-ion rechargeable battery by finite element method. *J. Power Sources* **2015**, *288*, 168–175.
- (96) Soni, R.; Robinson, J. B.; Shearing, P. R.; Brett, D. J.; Rettie, A. J.; Miller, T. S. Lithium-Sulfur Battery Diagnostics through Distribution of Relaxation Times Analysis. *Energy Storage Mater.* **2022**, *51*, 97–107.
- (97) Zhu, J.; Knapp, M.; Liu, X.; Yan, P.; Dai, H.; Wei, X.; Ehrenberg, H. Low-Temperature Separating Lithium-Ion Battery Interfacial Polarization Based on Distribution of Relaxation Times (DRT) of Impedance. *IEEE Trans. Transport. Electricif.* **2021**, *7* (2), 410–421.
- (98) Zhou, X.; Huang, J.; Pan, Z.; Ouyang, M. Impedance Characterization of Lithium-Ion Batteries Aging under High Temperature Cycling: Importance of Electrolyte-Phase Diffusion. *J. Power Sources* **2019**, *426*, 216–222.
- (99) Wang, J.; Huang, Q.; Li, W.; Wang, J.; Bai, Y.; Bai, Y.; Zhao, Y.; Li, X.; Zhang, J. Insight into the Origin of Pseudo Peaks Decoded by the Distribution of Relaxation Times/Differential Capacity Method for Electrochemical Impedance Spectroscopy. *J. Electroanal. Chem.* **2022**, *910*, 116176.
- (100) Qu, D.; Ji, W.; Qu, H. Probing process kinetics in batteries with electrochemical impedance spectroscopy. *Commun. Mater.* **2022**, *3*, 61.
- (101) Moškon, J.; Gaberšček, M. Transmission line models for evaluation of impedance response of insertion battery electrodes and cells. *J. Power Sources Adv.* **2021**, *7*, 100047.
- (102) ZView 3.5, Impedance/gain Phase Graphing and Analysis Software, Scribner Ass. Inc., <http://www.scribner.com/software/68-general-electrochemistr376-zview-for-windows/> (accessed February 9, 2023).
- (103) Python-assisted physics-based electrochemical impedance spectroscopy. <https://github.com/thuylinhpham/PyPhyEIS> (accessed February 9, 2023).
- (104) CNLS (Complex Nonlinear Least Squares), Immittance, Inversion, and Simulation Fitting Programs, J. R. MacDonald, <https://jrossmacdonald.com/levmlevmw/> (accessed February 9, 2023).
- (105) Nara, H.; Mukoyama, D.; Yokoshima, T.; Momma, T.; Osaka, T. Impedance Analysis with Transmission Line Model for Reaction Distribution in a Pouch Type Lithium-Ion Battery by Using Micro Reference Electrode. *J. Electrochem. Soc.* **2016**, *163*, 434–441.
- (106) Bernard, P.; Martinez, H.; Tessier, C.; Garitte, E.; Franger, S.; Dedryvere, R. Role of Negative Electrode Porosity in Long-Term Aging of NMC//Graphite Li-Ion Batteries. *J. Electrochem. Soc.* **2015**, *162*, 7096–7103.
- (107) Ogihara, N.; Itou, Y.; Sasaki, T.; Takeuchi, Y. Impedance Spectroscopy Characterization of Porous Electrodes under Different Electrode Thickness Using a Symmetric Cell for High-Performance Lithium-Ion Batteries. *J. Phys. Chem. C* **2015**, *119*, 4612–4619.
- (108) Dubarry, M.; Qin, N.; Brooker, P. Calendar aging of commercial Li-ion cells of different chemistries – A review. *Curr. Opin. Electrochem.* **2018**, *9*, 106–113.
- (109) Du, Y.; Fujita, K.; Shironita, S.; Sone, Y.; Hosono, E.; Asakura, D.; Umeda, M. Capacity fade characteristics of nickel-based lithium-ion secondary battery after calendar deterioration at 80 °C. *J. Power Sources* **2021**, *501*, 230005.
- (110) Shafiei Sabet, P.; Warnecke, A. J.; Meier, F.; Witzenhausen, H.; Martinez-Laserna, E.; Sauer, D. U. Non-invasive Yet Separate Investigation of Anode/Cathode Degradation of Lithium-Ion Batteries (Nickel–Cobalt–Manganese vs. Graphite) due to Accelerated Aging. *J. Power Sources* **2020**, *449*, 227369.
- (111) Schmitt, J.; Maheshwari, A.; Heck, M.; Lux, S.; Vetter, M. Impedance Change and Capacity Fade of Lithium Nickel Manganese Cobalt Oxide-Based Batteries During Calendar Aging. *J. Power Sources* **2017**, *353*, 183–194.
- (112) Li, J.; Zhang, J.; Zhang, X.; Yang, C.; Xu, N.; Xia, B. Study of the storage performance of a Li-ion cell at elevated temperature. *Electrochim. Acta* **2010**, *55*, 927–934.
- (113) Geisbauer, C.; Wohrl, K.; Koch, D.; Wihelm, G.; Schneider, G.; Schweiger, H. G. Comparative Study on the Calendar Aging Behavior of Six Different Lithium-Ion Cell Chemistries in Terms of Parameter Variation. *Energies* **2021**, *14*, 3358.
- (114) Keil, P.; Schuster, S. F.; Wihelm, J.; Travi, J.; Hauser, A.; Karl, R. C.; Jossen, A. Calendar Aging of Lithium-Ion Batteries. I. Impact of the Graphite Anode on Capacity Fade. *J. Electrochem. Soc.* **2016**, *163* (9), 1872–1880.
- (115) Kassem, M.; Bernard, J.; Revel, R.; Pelissier, S.; Duclaud, F.; Delacourt, C. Calendar Aging of a graphite/LiFePO₄ Cell. *J. Power Sources* **2012**, *208*, 296–305.
- (116) Zheng, Y.; He, Y.; Qian, K.; Li, B.; Wang, X.; Li, J.; Miao, C.; Kang, F. Effects of state of charge on the degradation of LiFePO₄/

- graphitebatteries during accelerated storage test. *J. Alloys Compd.* **2015**, *639*, 406–414.
- (117) Mendoza-Hernandez, O. S.; Hosono, E.; Asakura, D.; Matsuda, H.; Sayoko, S.; Umeda, M.; Sone, Y. Impact of calendar degradation on the Performance of LiFePO₄-Graphite Li-Ion Cells during Charge-Discharge Cycling at –5°C. *J. Electrochem. Soc.* **2019**, *166* (15), 3525–3530.
- (118) Zhang, L.; Liu, J.; Du, L.; Fan, P.; Xu, X.; Ma, Y.; Zuo, P.; Qu, B.; Yin, G.; Fu, Q.; et al. LiNi_{0.5}Co_{0.2}Mn_{0.3}O₂/Graphite batteries storing at high temperature: Capacity fading and raveling of aging mechanisms. *J. Power Sources* **2021**, *496*, 229858.
- (119) Zhang, L.; Liu, J.; Fan, P.; Du, L.; Ma, Y.; Qu, B.; Yin, G.; Fu, Q.; Yang, F.; et al. Unraveling the effect of short-term high-temperature storage on the performance and thermal stability of LiNi_{0.5}Co_{0.2}Mn_{0.3}O₂/Graphite Battery. *J. Power Sources* **2020**, *459*, 227842.
- (120) Dufek, E. J.; Tanim, T. R.; Chen, B. R.; Kim, S. Battery Calendar Aging and Machine Learning. *Joule* **2022**, *6*, 1363–1367.
- (121) Jaini, R. R.; Setzler, B. P.; Fuller, T. F. Investigating Changes in the Morphological Structure of High-Temperature, Calendar-Aged Li-Ion Cells. *J. Electrochem. Soc.* **2018**, *165* (13), A3125.
- (122) Yoshida, Y.; Takahashi, M.; Morikawa, S.; Ihara, C.; Katsukawa, H.; Shiratsuchi, T.; Yamaki, J. Degradation Mechanism and Life Prediction of Lithium-Ion Batteries. *J. Electrochem. Soc.* **2006**, *153* (6), 576–582.
- (123) Jalkanen, K.; Karppinen, J.; Skogstrom, L.; Laurila, T.; Nisula, M.; Vuorilehto, K. Cycle aging of commercial NMC/graphite pouch cells at different temperatures. *Appl. Energy* **2015**, *154*, 160–172.
- (124) Strehle, B.; Friedrich, F.; Gasteiger, H. A. A Comparative Study of Structural Changes during Long-Term Cycling of NCM-811 at Ambient and Elevated Temperatures. *J. Electrochem. Soc.* **2021**, *168*, No. 050512.
- (125) Zhu, X.; Revilla, R. I.; Jaguemont, J.; Mierlo, J. V.; Hubin, A. Insights into Cycling Aging of LiNi_{0.80}Co_{0.15}Al_{0.05}O₂ Cathode Induced by Surface Inhomogeneity: A Post-mortem Analysis. *J. Phys. Chem. C* **2019**, *123*, 30046–30058.
- (126) Raj, A.; Rodrigues, M. F.; Abraham, D. P. Rate-Dependent Aging Resulting from Fast Charging of Li-Ion Cells. *J. Electrochem. Soc.* **2020**, *167*, 120517.
- (127) Mussa, A. S.; Liivat, A.; Marzano, F.; Klett, M.; Philippe, B.; Tengstedt, C.; Lindbergh, G.; Edstrom, K.; Lindstrom, R. W.; Svens, P. Fast-charging effects on ageing for energy-optimized automotive LiNi_{1/3}Mn_{1/3}Co_{1/3}O₂/graphite prismatic lithium-ion cells. *J. Power Sources* **2019**, *422*, 175–184.
- (128) Zheng, H.; Li, X.; Huang, Z.; Yang, X.; Deng, J.; Zhang, G.; Tang, X. Investigation of the Performance and Recession Mechanisms of High-Nickel Ternary Lithium-Ion Batteries Under Artificial Aging Discharge Rates. *Energy Technol.* **2022**, *10*, 2200600.
- (129) Zhu, J.; Su, P.; Darma, M. S.; Hua, W.; Mereacre, L.; Liu-Theato, X.; Heere, M.; Sorensen, D. R.; Dai, H.; Wei, X.; et al. Multiscale investigation of discharge rate dependence of capacity fade for lithium-ion battery. *J. Power Sources* **2022**, *536*, 231516.
- (130) Qu, J.; Jiang, Z.; Zhang, J. Investigation on lithium-ion battery degradation induced by combined effect of current rate and operating temperature during fast charging. *J. Energy Storage* **2022**, *52*, 104811.
- (131) Leonardi, S. G.; Aloisio, D.; Brunaccini, G.; Stassi, A.; Ferraro, M.; Antonucci, V.; Sergi, F. Investigation on the ageing mechanism for a lithium-ion cell under accelerated tests: The case of primary frequency regulation service. *J. Energy Storage* **2021**, *41*, 102904.
- (132) Wu, Y.; Long, X.; Lu, J.; Wu, Y.; Zhou, R.; Liu, L. Effect of temperature on the high-rate pulse charging of lithium-ion batteries. *J. Electroanal. Chem.* **2022**, *922*, 116773.
- (133) Perumaram Rangarajan, S.; Barsukov, Y.; Mukherjee, P. P. Plating Energy as a Universal Descriptor to Classify Accelerated Cell Failure under Operational Extremes. *Cell Rep. Phys. Sci.* **2022**, *3*, 100720.
- (134) Carter, R.; Kingston, T. A.; Atkinson, R. W.; Parmananda, M.; Dubarry, M.; Fear, C.; Mukherjee, P. P.; Love, C. T. Directionality of thermal gradients in lithium-ion batteries dictates diverging degradation modes. *Cell Rep. Phys. Sci.* **2021**, *2*, 100351.
- (135) Liu, J.; Duan, Q.; Ma, M.; Zhao, C.; Sun, J.; Wang, Q. Aging Mechanisms and Thermal Stability of Aged Commercial 18650 Lithium Ion Battery Induced by Slight Overcharging Cycling. *J. Power Sources* **2020**, *445*, 227263.
- (136) Togasaki, N.; Yokoshima, T.; Oguma, Y.; Osaka, T. Prediction of Overcharge-Induced Serious Capacity Fading in Nickel Cobalt Aluminum Oxide Lithium-Ion Batteries Using Electrochemical Impedance Spectroscopy. *J. Power Sources* **2020**, *461*, 228168.
- (137) Liu, Y. D.; Xie, J. Failure Study of Commercial LiFePO₄ Cells in Overcharge Conditions Using Electrochemical Impedance Spectroscopy. *J. Electrochem. Soc.* **2015**, *162* (10), 2208–2217.
- (138) Liu, Y.; Liu, Q.; Li, Z.; Ren, Y.; Xie, J.; He, H.; Xu, F. Failure Study of Commercial LiFePO₄ Cells in over-Discharge Conditions Using Electrochemical Impedance Spectroscopy. *J. Electrochem. Soc.* **2014**, *161* (4), 620–632.
- (139) Deich, T.; Storch, M.; Steiner, K.; Bund, A. Effects of module stiffness and initial compression on lithium-ion cell aging. *J. Power Sources* **2021**, *506*, 230163.
- (140) Li, R.; Li, W.; Singh, A.; Ren, D.; Hou, Z.; Ouyang, M. Effect of external pressure and internal stress on battery performance and lifespan. *Energy Storage Mater.* **2022**, *52*, 395–429.
- (141) Mussa, A. S.; Klett, M.; Lindberg, G.; Lindstrom, R. W. Effects of external pressure on the performance and ageing of single-layer lithium-ion pouch cells. *J. Power Sources* **2018**, *385*, 18–26.
- (142) Tian, Y.; Lin, C.; Li, H.; Du, J.; Xiong, R. Detecting undesired lithium plating on anodes for lithium-ion batteries – A review on the in-situ methods. *Applied Energy* **2021**, *300*, 117386.
- (143) Petzl, M.; Kasper, M.; Danzer, M. A. Lithium plating in a commercial lithium-ion battery—A low-temperature aging study. *J. Power Sources* **2015**, *275*, 799–807.
- (144) Schuster, S. F.; Bach, T.; Elena, F.; Muller, J.; Brand, M.; Sextl, G.; Jossen, A. Nonlinear Aging Characteristics of Lithium-Ion Cells under Different Operational Conditions. *J. Energy Storage* **2015**, *1*, 44–53.
- (145) Chen, X.; Li, L.; Liu, M.; Huang, T.; Yu, A. Detection of Lithium Plating in Lithium-ion Batteries by Distribution Relaxation Times. *J. Power Sources* **2021**, *496*, 229867.
- (146) Gargh, P.; Sarkar, A.; Lui, Y.; Shen, S.; Hu, C.; Hu, S.; Nlebedim, I. C.; Shrotriya, P. Correlating Capacity Fade with Film Resistance Loss in Fast Charging of Lithium-Ion Battery. *J. Power Sources* **2021**, *485*, 229360.
- (147) Schindler, S.; Bauer, M.; Petzl, M.; Danzer, M. A. Voltage relaxation and impedance spectroscopy as *in-operando* methods for the detection of lithium plating on graphitic anodes in commercial lithium-ion cells. *J. Power Sources* **2016**, *304*, 170–180.
- (148) Xu, L.; Yang, Y.; Xiao, Y.; Cai, W.; Yao, Y.; Chen, X.; Yan, C.; Yuan, H.; Huang, J. In-situ Determination of Onset Lithium Plating for Safe Li-ion Batteries. *J. Energy Chem.* **2022**, *67*, 255–262.
- (149) Koleti, U. R.; Dinh, T. Q.; Macro, J. A New On-Line Method for Lithium Plating Detection in Lithium-Ion Batteries. *J. Power Sources* **2020**, *451*, 227798.
- (150) Koseoglou, M.; Tsoumias, E.; Ferentinou, D.; Jabbour, N.; Papagiannis, D.; Mademlis, C. Lithium Plating Detection Using Dynamic Electrochemical Impedance Spectroscopy in Lithium-Ion Batteries. *J. Power Sources* **2021**, *512*, 230508.
- (151) Xu, L.; Xiao, Y.; Yang, Y.; Yang, S.; Chen, X.; Xu, R.; Yao, Y.; Cai, W.; Yan, C.; Huang, J. Q.; et al. Operando Quantified Lithium Plating Determination Enabled by Dynamic Capacitance Measurement in Working Li-Ion Batteries. *Angew. Chem., Int. Ed.* **2022**, *61*, e202210365.
- (152) Peled, E. The Electrochemical Behavior of Alkali and Alkaline Earth Metals in Nonaqueous Battery Systems—The Solid Electrolyte Interphase Model. *J. Electrochem. Soc.* **1979**, *126* (12), 2047–2051.
- (153) Aurbach, D.; Levi, M. D.; Gamulski, K.; Markovsky, B.; Salitra, G.; Levi, E.; Heider, U.; Heider, L.; Oesten, R. Capacity fading of Li_xMn₂O₄ spinel electrodes studied by XRD and electroanalytical techniques. *J. Power Sources* **1999**, *81*–82, 472–479.

- (154) Wu, J. X.; Ihsan-Ul-Haq, M.; Chen, Y. M.; Kim, J. K. Understanding solid electrolyte interphases: Advanced characterization techniques and theoretical simulations. *Nano Energy* **2021**, *89*, 106489.
- (155) Sun, C.; Ji, X.; Weng, S.; Li, R.; Huang, X.; Zhu, C.; Xiao, X.; Deng, T.; Fan, L.; Chen, L.; et al. 50C Fast-Charge Li-Ion Batteries using a Graphite Anode. *Adv. Mater.* **2022**, *34*, 2206020.
- (156) Solchenbach, S.; Huang, X. Y.; Pitzl, D.; Landesfeind, J.; Gasteiger, H. A. Monitoring SEI Formation on Graphite Electrodes in Lithium-Ion Cells by Impedance Spectroscopy. *J. Electrochem. Soc.* **2021**, *168*, 110503.
- (157) Ehteshami, N.; Ibing, L.; Stoltz, L.; Winter, M.; Paillard, E. Ethylene Carbonate-Free Electrolytes for Li-Ion Battery: Study of the Solid Electrolyte Interphases Formed on Graphite Anodes. *J. Power Sources* **2020**, *451*, 227804.
- (158) Lu, P.; Li, C.; Schneider, E. W.; Harris, S. J. Chemistry, Impedance, and Morphology Evolution in Solid Electrolyte Interphase Films during Formation in Lithium Ion Batteries. *J. Phys. Chem. C* **2014**, *118*, 896–903.
- (159) Wang, P.; Yan, D.; Wang, C. Y.; Ding, H.; Dong, H.; Wang, J.; Wu, S.; Cui, X.; Li, C.; Zhao, D.; et al. Study of the formation and evolution of solid electrolyte interface via in-situ electrochemical impedance spectroscopy. *Appl. Surf. Sci.* **2022**, *596*, 153572.
- (160) Steinhauer, M.; Risse, S.; Wagner, N.; Friedrich, K. A. Investigation of the Solid Electrolyte Interphase Formation at Graphite Anodes in Lithium-Ion Batteries with Electrochemical Impedance Spectroscopy. *Electrochim. Acta* **2017**, *228*, 652–658.
- (161) Qu, H.; Zhang, X.; Ji, W.; Zheng, D.; Qu, D. Impedance Investigation of the High Temperature Performance of the Solid-Electrolyte-Interface of a Wide Temperature Electrolyte. *J. Colloid Interface Sci.* **2022**, *608*, 3079–3086.
- (162) Xu, H.; Li, Z.; Liu, T.; Han, C.; Guo, C.; Zhao, H.; Li, Q.; Lu, J.; Amine, K.; Qiu, X. Impacts of Dissolved Ni²⁺ on the Solid Electrolyte Interphase on a Graphite Anode. *Angew. Chem., Int. Ed.* **2022**, *61*, e202202894.
- (163) Broussely, M.; Herreyre, S.; Biensan, P.; Kasztejna, P.; Nechev, K.; Staniewicz, R. J. Aging Mechanism in Li Ion Cells and Calendar Life Predictions. *J. Power Sources* **2001**, *97–98*, 13–21.
- (164) Ploehn, H. J.; Ramadass, P. L.; White, R. E. Solvent Diffusion Model for Aging of Lithium-Ion Battery Cells. *J. Electrochem. Soc.* **2004**, *151* (3), 456–462.
- (165) Safari, M.; Morcrette, M.; Teyssot, A.; Delacourt, C. Multimodal Physics-Based Aging Model for Life Prediction of Li-Ion Batteries. *J. Electrochem. Soc.* **2009**, *156* (3), 145–153.
- (166) Chen, C.; Mukherjee, P. P. Probing the Morphological Influence on Solid Electrolyte Interphase and Impedance Response in Intercalation Electrodes. *Phys. Chem. Chem. Phys.* **2015**, *17*, 9812.
- (167) Single, F.; Horstmann, B.; Latz, A. Theory of Impedance Spectroscopy for Lithium Batteries. *J. Phys. Chem. C* **2019**, *123*, 27327–27343.
- (168) Drvarić Talian, S.; Bobnar, J.; Sinigoj, A. R.; Humar, I.; Gaberšček, M. Transmission Line Model for Description of the Impedance Response of Li Electrodes with Dendritic Growth. *J. Phys. Chem. C* **2019**, *123*, 27997–28007.
- (169) Santos, C. S.; Botz, A.; Bandarenka, A. S.; Ventosa, E.; Schuhmann, W. Correlative Electrochemical Microscopy for the Elucidation of the Local Ionic and Electronic Properties of the Solid Electrolyte Interphase in Li-Ion Batteries. *Angew. Chem., Int. Ed.* **2022**, *61*, e202202744.
- (170) Teo, L.; Subramanian, V.; Schwartz, D. Dynamic Electrochemical Impedance Spectroscopy of Lithium-ion Batteries: Revealing Underlying Physics through Efficient Joint Time Frequency Modeling. *J. Electrochem. Soc.* **2021**, *168*, No. 010526.
- (171) Jiang, B.; Gent, W.; Mohr, F.; Das, S.; Berliner, M. D.; Forsuelo, M.; Zhao, H.; Attia, P. M.; Grover, A.; Herring, P. K.; et al. Bayesian Learning for Rapid Prediction of Lithium-Ion Battery-Cycling Protocols. *Joule* **2021**, *5*, 3187–3203.
- (172) Xu, J.; Mi, C.; Cao, B.; Cao, J. A new method to estimate the state of charge of lithium-ion batteries based on the battery impedance model. *J. Power Sources* **2013**, *233*, 277–284.
- (173) Luo, K.; Chen, X.; Zheng, H.; Shi, Z. A Review of Deep Learning Approach to Predicting the State of Health and State of Charge of Lithium-Ion Batteries. *J. Energy Chem.* **2022**, *74*, 159–173.
- (174) Shu, X.; Shen, S.; Shen, J.; Zhang, Y.; Li, G.; Chen, Z.; Liu, Y. State of Health Prediction of Lithium-Ion Batteries Based on Machine Learning: Advances and Perspectives. *iScience* **2021**, *24*, 103265.
- (175) Sui, X.; He, S.; Vilse, S. B.; Meng, J. H.; Teodorescu, R.; Stroe, D. I. A Review of Non-Probabilistic Machine Learning-Based State of Health Estimation Techniques for Lithium-Ion Battery. *Applied Energy* **2021**, *300*, 117346.
- (176) Liu, J.; Duan, Q.; Qi, K.; Sun, J.; Wang, Z.; Wang, Q. Capacity Fading Mechanisms and State of Health Prediction of Commercial Lithium-Ion Battery in Total Lifespan. *J. Energy Storage* **2022**, *46*, 103910.
- (177) Pizarro-Carmona, V.; Cortes-Carmona, M.; Palma-Behnke, R.; Calderon-Munoz, W.; Orchard, M. E.; Estevez, P. An Optimized Impedance Model for the Estimation of the State-of-Charge of a Li-Ion Cell: The Case of a LiFePO₄. *Energies* **2019**, *12*, 681.
- (178) Locorotondo, E.; Cultrera, V.; Pugi, L.; Berzi, L.; Pierini, M.; Lutzemberger, G. Development of a Battery Real-Time State of Health Diagnosis based on Fast Impedance Measurements. *J. Energy Storage* **2021**, *38*, 102566.
- (179) Zhu, J.; Zhang, Q.; Mereacre, L. D.; Wang, X.; Jiang, B.; Dai, H.; Wei, X.; Knapp, M.; Ehrenberg, H. Alternating Current Impedance Probing Capacity of Lithium-Ion Battery by Gaussian Process Regression. *Energy Technol.* **2022**, *10*, 2200437.
- (180) Jiang, B.; Zhu, J.; Wang, X.; Wei, X.; Shang, W.; Dai, H. A comparative study of different features extracted from electrochemical impedance spectroscopy in state of health estimation for lithium-ion batteries. *Appl. Energy* **2022**, *322*, 119502.
- (181) Li, W.; Chen, J.; Quade, K.; Luder, D.; Gong, J.; Sauer, D. U. Battery degradation diagnosis with field data, impedance-based modeling and artificial intelligence. *Energy Storage Mater.* **2022**, *53*, 391–403.
- (182) Babaeiyazdi, I.; Rezaei-Zare, A.; Shokrzadeh, S. Transfer Learning with Deep Neural Network for Capacity Prediction of Li-ion Batteries Using EIS Measurement. *IEEE Trans. Transport. Electrific.* doi: 20221 (accessed February 9, 2023).
- (183) Penjuru, N. M. H.; Reddy, G. V.; Nair, M. R.; Sahoo, S.; Mayank; Jiang, J.; Ahmed, J.; Wang, H.; Roy, T. Machine Learning Aided Predictions for Capacity Fade of Li-Ion Batteries. *J. Electrochem. Soc.* **2022**, *169*, No. 050535.